



Establishing the temperature and orientation dependence of the threshold displacement energy in ThO₂ via molecular dynamics simulations

December 2024

Changing the World's Energy Future

Lin-Chieh Yu, Miaomiao Jin, Marat Khafizov, Yongfeng Zhang, Shuxiang Zhou, David H Hurley



DISCLAIMER

This information was prepared as an account of work sponsored by an agency of the U.S. Government. Neither the U.S. Government nor any agency thereof, nor any of their employees, makes any warranty, expressed or implied, or assumes any legal liability or responsibility for the accuracy, completeness, or usefulness, of any information, apparatus, product, or process disclosed, or represents that its use would not infringe privately owned rights. References herein to any specific commercial product, process, or service by trade name, trade mark, manufacturer, or otherwise, does not necessarily constitute or imply its endorsement, recommendation, or favoring by the U.S. Government or any agency thereof. The views and opinions of authors expressed herein do not necessarily state or reflect those of the U.S. Government or any agency thereof.

**Establishing the temperature and orientation
dependence of the threshold displacement energy in
ThO₂ via molecular dynamics simulations**

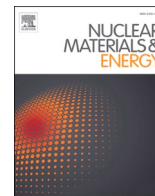
**Lin-Chieh Yu, Miaomiao Jin, Marat Khafizov, Yongfeng Zhang, Shuxiang Zhou,
David H Hurley**

December 2024

**Idaho National Laboratory
Idaho Falls, Idaho 83415**

<http://www.inl.gov>

**Prepared for the
U.S. Department of Energy
Under DOE Idaho Operations Office
Contract TET1 EFRC**



Establishing the temperature and orientation dependence of the threshold displacement energy in ThO₂ via molecular dynamics simulations

Lin-Chieh Yu^{a,b}, Shuxiang Zhou^c, Miaomiao Jin^d, Marat Khafizov^e, David Hurley^c, Yongfeng Zhang^{b,*}

^a Department of Material Science and Engineering, University of Wisconsin-Madison, Madison, WI 53706, USA

^b Department of Nuclear Engineering and Engineering Physics, University of Wisconsin-Madison, Madison, WI 53706, USA

^c Idaho National Laboratory, Idaho Falls, ID 83415, USA

^d Department of Nuclear Engineering, The Pennsylvania State University, University Park, PA 16802, USA

^e Department of Mechanical and Aerospace Engineering, The Ohio State University, Columbus, OH 43210, USA

ARTICLE INFO

Keywords:

ThO₂
Threshold displacement energy
Molecular dynamics
Temperature dependence
Orientation dependence
Coulomb interaction

ABSTRACT

ThO₂ is a promising fuel for next-generation nuclear reactors. As a critical quantity measuring its radiation tolerance, the dependence of the threshold displacement energy on temperature and crystal orientation in ThO₂ is unclear and established using comprehensive molecular dynamics simulations in this work. For both Th and O primary knock-on atoms (PKAs), the thresholds, denoted as E_d^{Th} and E_d^O , respectively, are calculated using two different interatomic potentials. Similar temperature and orientation dependence are observed, albeit with some quantitative differences. While on average over all orientations, higher energy is required for Th PKAs than O PKAs to displace atoms, the polar-averaged E_d^{Th} is significantly lower than that for E_d^O . Further, E_d^{Th} and E_d^O show different crystal orientation dependence and temperature dependence. Notably, the cubic symmetry in the fluorite structure is followed by E_d^{Th} , but does not hold for E_d^O because of the existence of two sublattices. The much higher average E_d^O than E_d^{Th} and their different temperature dependence are interpreted by the distinct recombination rates of Th and O Frenkel pairs in thermal spikes, resulting from the substantially lower migration barriers of O vacancies and interstitials. The recombination of O vacancies and interstitials, both of which are charged, is further enhanced by the Coulomb interaction at small Frenkel pair separations. The new findings are discussed for their generality in fluorite-structured oxides by comparing the results in ThO₂ and UO₂.

Introduction

Nuclear power plays a critical role in global energy production. Essential to nuclear energy production is nuclear fuel. Most current nuclear reactors are light water reactors and utilize UO₂, which is a well-developed commercial fuel. With a similar crystal structure to UO₂, thorium (ThO₂) has been proposed as an alternative proliferation-resistant nuclear fuel because of several advantages over UO₂, including higher abundance, higher thermal conductivity, and a lower coefficient of thermal expansion [1,2]. Thorium and thorium-based fuels have been utilized in combination with fissile fuels in breeder reactor systems to enlarge the fissile material resources [3]. ThO₂-based fuel has been assessed in the pressurized heavy water reactor in CANDU (CANada Deuterium Uranium) reactor to demonstrate its advantages in normal

operation and waste management [4,5]. It is also widely used as a non-radioactive surrogate material for UO₂ in research because they share the same crystal structure and similar ionic bonding nature [6]. In both UO₂ and ThO₂, the thermophysical and thermomechanical properties can be significantly influenced by the lattice defects induced by high-energy particle irradiation, such as neutrons, fission fragments, and ions. For instance, recent research has demonstrated a significant reduction in thermal conductivity attributed to defect clustering and increased defect concentration [7,8]. Understanding the primary production, thermal diffusion, and long-term evolution of irradiation-induced defects, termed radiation damage, is imperative for the safe and economical utilization of oxide fuels.

The development of radiation damage and the consequent degradation in fuel properties start with primary defect production, which

* Corresponding author.

E-mail address: y Zhang@wisc.edu (Y. Zhang).

<https://doi.org/10.1016/j.nme.2024.101774>

Received 24 February 2024; Received in revised form 24 September 2024; Accepted 15 October 2024

Available online 20 October 2024

2352-1791/© 2024 The Author(s). Published by Elsevier Ltd. This is an open access article under the CC BY-NC license (<http://creativecommons.org/licenses/by-nc/4.0/>).

refers to the type and amount of defects produced in displacement cascades. When a high-energy particle is introduced into crystalline solids, it is scattered and partially transfers its kinetic energy to primary knock-on atoms (PKAs). When the kinetic energy passed to a PKA exceeds a certain threshold, the PKA and its neighboring atoms will be displaced from their lattice sites. Meanwhile, the local temperature will increase substantially with the formation of a local thermal spike. The thermal spike lasts for a few picoseconds (ps) until the local heat is dissipated into the surrounding materials. Most of the displaced atoms will recover to regular lattice during the thermal spike via relaxation of disordered crystal structure and correlated recombination of defects of the opposite type. The defects that survive the thermal spike, termed primary defects, are responsible for long-term defect accumulation and property degradation [9,10]. To quantify the number of primary defects resulting from a PKA event, the threshold displacement energy, E_d , is introduced and defined as the threshold energy transferred to a PKA that results in the formation of one (or more) stable Frenkel pair (FP), i.e., a pair of vacancy and interstitial. Since its introduction, E_d has been commonly used to quantify the irradiation dose a given material has been subjected to, using the Norgett-Robinson-Torrens (NRT) or the Kinchin-Pease (KP) models [11,12] or widely used software such as SRIM [13].

As E_d is defined upon primary defect production within a timescale of a few ps, direct determination of E_d using experiments is difficult. Often, it is indirectly derived from changes in material microstructure and properties caused by long-term defect accumulation [14,15]. The measured results are subjected to errors caused by uncorrelated defect recombination in the laboratory timescale. Alternatively, atomistic calculations such as classical molecular dynamics (MD) and *ab initio* MD (AIMD) have been commonly adopted to determine E_d , in the merit of their capabilities of resolving the dynamic defect production process in the atomic length scale and the timescale of ps. However, accurate determination of E_d is still challenging because of its ambiguous definition. Several different definitions have been utilized in the literature for computing E_d , including the minimum energy to create defects at the PKA site [16,17], the minimum energy to displace atoms beyond a cutoff distance [18], and the minimum energy to create FPs [19–21], and these definitions will lead to distinct results. Further, E_d depends on temperature and the crystal orientation along which the PKA is displaced. Restricted by crystal symmetry, it's relatively easier to displace an atom along certain orientations than others. In metals, a general trend has been established that E_d is higher along high-index orientations than along low-index ones [22–24]. The trend is less clear for ceramics because of insufficient data [15]. While many computational works report either polar-averaged E_d over a few low-index or random orientations, the experimentally measured ones based on detectable defects may correspond to the lowest E_d among all orientations, making it hard to compare the computed and experimentally measured values. Furthermore, temperature affects E_d and its measurement in several ways. On the one hand, increasing temperature weakens the atomic bonds, making it easier to permanently displace atoms and leading to decreasing E_d . Previous studies in metals have suggested steadily decreasing E_d with increasing temperature [15,25]. On the other hand, increasing temperature promotes correlated recombination during thermal spike [19], reducing the probability of stable FP formation and increasing E_d . A recent study in TiO₂ using MD has shown that E_d^O increases substantially from 50 K to 750 K while E_d^{Ti} exhibits a weak temperature dependence [19]. Therefore, both the orientation and temperature dependence of E_d need to be established to have a clear understanding on primary defect production. Further, defect production in a thermal spike is highly stochastic. Statistical significance must be achieved to obtain reliable data for E_d .

In the literature, E_d in ThO₂ has been determined only in a couple of computational studies with no experimental data. Rahman et al. [26] employed MD simulations with a 5 keV PKA energy and the Kinchin-Pease model to determine E_d . Without distinguishing the PKA type,

they found that E_d increased from 54.7 to 74.9 eV when temperature was increased from 300 to 1500 K. Elevated temperature led to the creation of more defects and accelerated the efficiency of defect recombination, with a combined effect of ultimately reducing the number of residual defects. It's also suggested in this study that thermally-activated diffusion plays a major role in defect recombination. Xiao et al. [17] utilized AIMD method to simulate low-PKA-energy radiation at 100 K and determined E_d based on the criterion of whether the PKA atom is displaced from its original site at 1 ps. The computed E_d^{Th} is in the range of 53.5 to 61.5 eV and E_d^O in the range of 17.5 to > 100 eV for four different orientations, [100], [110], [111], and [112], indicating a strong dependence on crystal orientation. While these studies have provided useful insights, the limited data obtained thus far are insufficient to determine the polar-averaged E_d^O and E_d^{Th} over all orientations and establish their dependence on orientation and temperature.

Compared to ThO₂, there have been more calculations of E_d in UO₂ [16,21,27–30]. As ThO₂ and UO₂ share the same crystal structure, insights obtained with UO₂ may be transferrable to ThO₂ [6]. Meis and Chartier [27] calculated E_d using static calculations with an ionic interatomic potential for UO₂. They reported a higher average E_d for U, denoted as E_d^U , of about 50 eV, than the average E_d^O of about 20 eV. A similar trend was reported by Jiang et al. [16] using AIMD, with an average E_d^U of about 46.96 eV and an average E_d^O of about 25.56 eV based on the data from a few low-index orientations. The threshold was determined by whether the displaced PKA returned to its original lattice site at 1 ps. The trend reported by Meis and Chartier and Jiang et al. is consistent with the experimental work for UO₂ by Soullard and Alamo [29,30], which reported a E_d^U of about 40 eV and a E_d^O of about 20 eV using high-voltage electron microscopy (HVEM). In a recent MD study in UO₂ at 1500 K with several interatomic potentials, Dacus et al. [21] reported an average E_d^U of about 60 eV, considerably lower than the average E_d^O , which is above 200 eV, when E_d was determined using the criterion that the defect formation probability (DFP, the probability of forming stable FPs) exceeds 50%. In contrast, when the criterion that the PKA atom is displaced from its original site was used, E_d^U was found to fall within the range of 20–35 eV, higher than E_d^O in the range of 10–15 eV. The contradicting data in the literature makes it unclear how E_d depends on the PKA type, i.e., whether E_d^U is higher or lower than E_d^O . The temperature dependence of E_d has not been established as only a single temperature is studied in the previous AIMD and MD simulations. Similar to the case of ThO₂, only selected crystal orientations have been studied, which is insufficient to establish the full orientation dependence. Interestingly, different orientation dependence has been reported in UO₂ compared with ThO₂. In the AIMD work in ThO₂ by Xiao et al. [17], E_d^{Th} follows the order [110] < [100] < [112] < [111], while E_d^O follows the order [100] < [112] < [110] < [111]. With a similar AIMD approach used by Jiang et al. in UO₂, E_d^U follows the order [100] < [111] < [112] < [110], while E_d^O follows the order [100] < [112] < [110] < [111]. Note that in both UO₂ and ThO₂, E_d for cation and anion have been shown to have different orientation dependence.

In this work, comprehensive molecular dynamics simulations are carried out to compute the threshold displacement energy in ThO₂, to establish the dependence of E_d on PKA type, orientation, and temperature. The FP formation energy and defect migration barriers are also computed to help understand the dependence of E_d on PKA type. The results show that E_d^O is significantly affected by correlated recombination in the thermal spike, which is further promoted by the Coulomb attraction between O vacancies and interstitials of opposite charge. A hidden asymmetry in fluorite-structured oxides is identified for the O sublattice, which has been ignored and must be considered for establishing the orientation dependence of E_d^O .

Methodology

Interatomic potentials

The molecular dynamics (MD) simulations are conducted using the LAMMPS [31] package. Two empirical potentials, previously developed by Cooper et al. [32] and Zhou et al. [33], are employed to assess uncertainties associated with the choice of potential. Both potentials utilize a many-body Embedded Atom Method (EAM) description [34] with Morse [35], Buckingham [36], and Coulomb potential forms to capture the inter-particle interaction within the system. Experimental and ab-initio validation confirmed that these potentials reliably reproduce thermophysical properties under high-temperature conditions [32,33,37]. The selection of the Cooper potential is based on its exceptional performance in predicting thermodynamic properties and defect formation energies. In comparison, the Zhou potential, which was recently developed following the analytical expression of the Cooper potential with additional DFT calculations, exhibits improved performance in predicting the phonon spectra and thermal conductivity, while the performance on defect properties has not been assessed. This deliberate choice aims to leverage the strengths of each potential to avoid the dependence of the general trends on the choice of interatomic potential. Both potentials utilize fixed, non-formal charges to simulate the Coulomb interaction in the ThO_2 system. The Cooper potential employs charge values of +2.2208 for cations and -1.1104 for anions, while the Zhou potential uses +2.5116 for cations and -1.2556 for anions. To mitigate the unrealistic forces stemming from the Buckingham term at short distances, it is bridged with the Ziegler-Biersack-Littmark (ZBL) repulsive potential [38] using a sine function with the cutoffs at 0.5 Å and 1.5 Å. The sine function is selected as the bridging function due to its smooth nature and zero first-order derivatives at both cutoffs. The ZBL potential fully replaces the Buckingham term below 0.5 Å and vanishes beyond 1.5 Å. More details about bridging the ZBL potential are provided in Section S1 of [Supplementary Materials](#).

Threshold displacement energy calculation

Simulated irradiation with low PKA energies from 10 to 300 eV is utilized to compute E_d . To save computation cost, an increment of 10 eV is used from 10-100 eV, and 50 eV from 100-300 eV, to allow for a detailed investigation of the relatively high E_d^O . The simulation cell contains $10 \times 10 \times 10$ conventional fluorite cells with 12,000 atoms. Periodic boundary conditions are imposed in all directions. The time-steps are either 2.5 fs or determined by using a maximum atomic displacement of 0.1 Å, whichever is smaller. This can maximize simulation efficiency while preventing unrealistically large atomic displacement when PKAs are introduced. The system is initialized at 0 K and then equilibrated at the desired temperature with zero pressure at the boundaries. Four temperatures, 100 K, 500 K, 1000 K, and 1500 K, are considered to study the temperature dependence. The highest temperature, 1500 K, is comparable to the upper bound of the fuel operation temperature in nuclear reactors [5,39]. After equilibration, a PKA, either Th or O, is selected with its velocity scaled in accordance with the desired PKA energy and redirected to a random direction. The simulation cell is then relaxed for 5 ps with the NVT ensemble. The temperature is controlled by a velocity rescaling thermostat every 100 MD steps to remove the excess heat. Each time the system temperature is rescaled toward the target temperature by 10% ($\Delta T = 10\%(T_{\text{current}} - T_{\text{target}})$), to minimize the impact of thermostat on defect production. A comparison of the rescaling approach and the often-used heat sink approach for temperature control has been made and described in Section S5 of [Supplementary Materials](#). The choice of 5 ps follows the recent study in UO_2 [21]. As has been pointed out in Robinson et al. [19], a short thermal spike lifetime may overestimate E_d by suppressing correlated recombinations, while a long thermal spike time may underestimate E_d because of uncorrelated recombination. After relaxation, the system is quenched to 0 K to determine whether stable FPs are generated by adopting the dynamic quenching algorithm [40]. The system temperature is quenched down to 0 K within 1 ps to prevent significant changes in the defect structures during quenching. As an example, the maximum atomic displacement during quenching is found to be 1.2×10^{-4} Å for Th

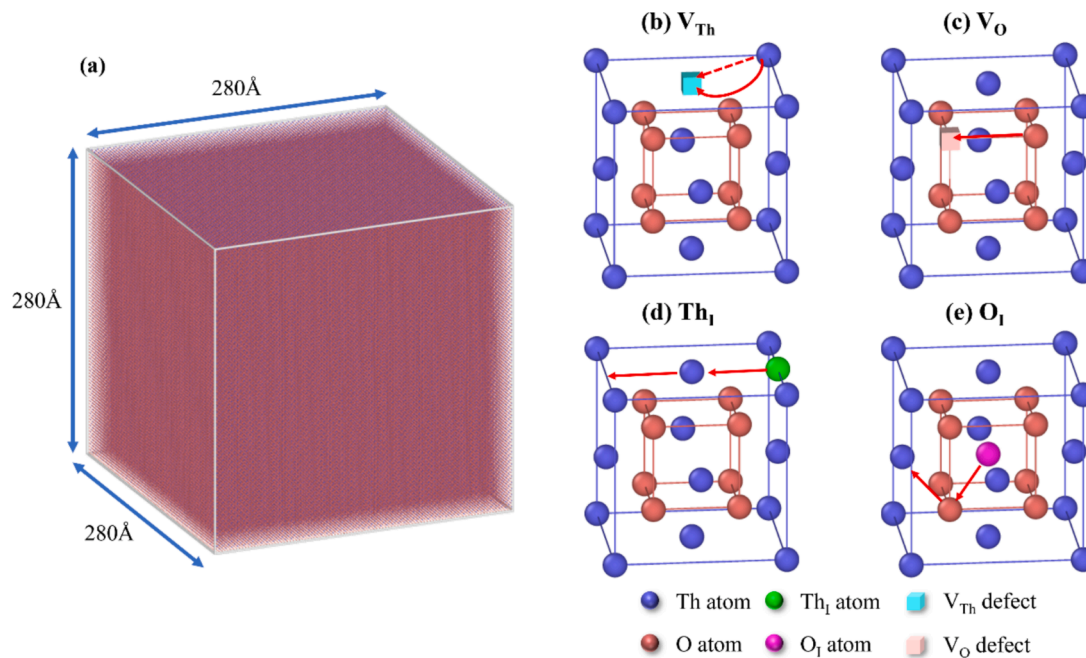


Fig. 1. (a) A $50 \times 50 \times 50 a_0^3$ ThO_2 supercell, and schematic views of the migration paths for (b) V_{Th} , (c) V_{O} , (d) Th_i , and (e) O_i . The solid arrows show the atomic displacements during diffusion. In (b), the dashed red line represents the prescribed straight path along $\langle 110 \rangle$, and the solid curve traces the actual path given by NEB. The thorium and oxygen vacancies are indicated as cyan cubes and pink cubes. The thorium and oxygen interstitials are indicated as green spheres and magenta spheres. (For interpretation of the references to colour in this figure legend, the reader is referred to the web version of this article.)

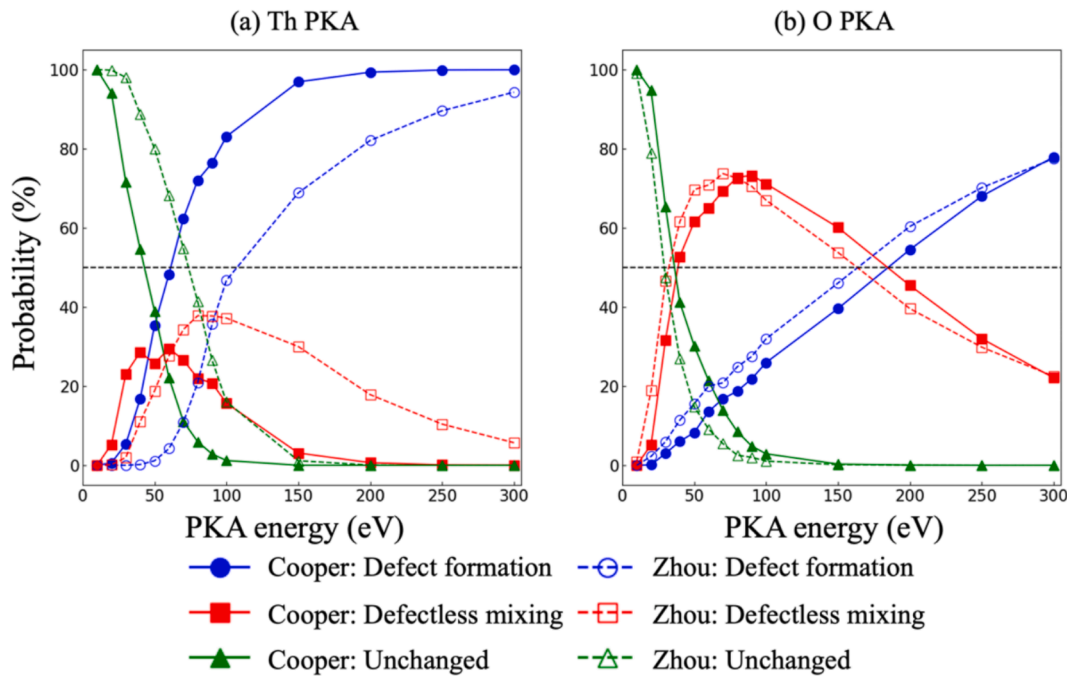


Fig. 2. The probabilities for defect formation, defectless displacement, and unchanged configurations as a function of PKA energy at 1500 K obtained with (a) Th PKA and (b) O PKA for the Cooper potential (solid line) and Zhou potential (dashed line).

PKA and 0.88 Å for O PKA in two simulations at 1500 K with a PKA energy of 300 eV. For each combination of PKA energy and temperature, 2,000 independent simulations are conducted with random PKA directions, to comprehensively explore the orientation dependence.

The defect characterization and visualization are accomplished using the OVITO package [41]. The Wigner-Seitz defect analysis [42] is performed to determine the numbers and positions of vacancies and interstitials for both Th and O. Based on the analysis, the final configurations are categorized into three groups:

- Defect formation: One or more stable Frenkel pairs (FPs) are generated.
- Defectless mixing: Atoms are displaced from their original sites but recover to other lattice sites without FP formation. The perfect crystal cell is recovered after the thermal spike.
- Unchanged: All atoms remain at their original sites after the thermal spike with neither FPs nor mixing.

For each combination of PKA energy and temperature, the number of cases in each group is divided by the total number of simulations to obtain the corresponding probability. For example, the defect formation probability (DFP) is computed as the total number of simulations with defect formation (group (a)), $N_{\text{defectformation}}$, divided by the total number of simulations, $N_{\text{simulation}}$, as $DFP = \frac{N_{\text{defectformation}}}{N_{\text{simulation}}}$. The atomic displacement probability (ADP) is computed as the sum of the numbers of simulations in group (a) for defect formation and group (b) for defectless mixing, divided by the total number of simulations because atoms must be displaced to generate FPs. Following the recent study in UO_2 [21], here we define E_d by the PKA energy at which the DFP reaches 50%. Similarly, a threshold mixing energy, E_m , can be defined by the PKA energy at which the ADP reaches 50%. As such, one data point for DFP and one for ADP will be generated using all 2000 simulations for each unique combination of temperature and PKA energy, without giving an error bar for E_d or E_m . A conservative estimate of the error bar has been carried out using sub-groups of the total simulations (i.e., smaller $N_{\text{simulations}}$) and is described in the Supplementary Materials. As shown in Tables S4-S7, the error for average E_d decreases with $N_{\text{simulation}}$ generally and is within 1 eV

for Th PKAs and 14 eV for O PKA using $N_{\text{simulation}} = 1000$. We note that this error only accounts for the statistical error in the MD simulations, but not the possible inaccuracy from the interatomic potentials and the interpolation errors in the DFP and ADP curves. In addition to the threshold defined based on DFP, we have also quantified E_d and E_m based on the average number of FPs generated and the average number of atoms displaced. In this case, E_d (E_m) is defined by the PKA energy at which by average 1.0 FP is generated (1.0 atom is displaced). For clarity, E_d and E_m defined by these criteria are presented in Table S1 and Table S2 in the Supplementary Materials.

Defect formation energy and migration barrier

The formation energies of Th and O FPs and the migration barriers of Th and O vacancies and interstitials are computed, to investigate their possible impact on threshold displacement energy. As both Th and O vacancies and interstitials are charged, one FP is created to maintain charge neutrality in all calculations. To minimize the Coulomb interaction between the vacancy and interstitial, a large cell of a $50 \times 50 \times 50 a_0^3$ with 1,500,000 atoms is utilized, as shown in Fig. 1(a); a_0 is the lattice parameter. Starting with a periodic cell with zero external pressure at 0 K, a Th FP is created by displacing a Th atom to an octahedral site (i.e., the center of the fluorite conventional cell) over 3 nm away at which the FP formation energy is expected to converge, as shown by previous DFT calculations [43] and our MD calculations (See Figure S10 in Supplementary Materials). An O FP is created in the same way. The octahedral site has been shown to be the stable interstitial configuration for both Th and O interstitials by density functional theory (DFT) calculations [44]. This large FP separation distance, i.e., the distance between the vacancy and interstitial forming the FP, is utilized to converge FP formation energies over distance. The defected structure is then relaxed with the energy and force tolerances set at 1×10^{-15} and 1×10^{-18} eV/Å. The FP formation energy, E_{FP} , is computed as the excess energy of the defected cell in reference to the perfect cell, as $E_{FP} = \frac{E_{\text{defect}}^{\text{total}} - E_{\text{perfect}}^{\text{total}}}{N_{\text{defect}}}$; here $E_{\text{defect}}^{\text{total}}$ and $E_{\text{perfect}}^{\text{total}}$ are the total energies of the cells with and without an FP, respectively. The same theoretical model is used for both Th and O FPs.

The migration energies of point defects are calculated using the

Table 1
Average threshold displacement energy E_d in ThO₂, in the unit of eV.

Source	E_d^{Th}				E_d^O		
	MD Cooper	MD Zhou	MD [26]	AIMD [17]	MD Cooper	MD Zhou	AIMD [17]
100 K	75.92	128.09		54.5	137.87	110.59	> 49.17
300 K			54.74				
500 K	72.48	127.51			147.22	120.73	
900 K			71.40				
1000 K	66.19	121.08			171.10	156.48	
1500 K	61.21	107.35	74.97		184.90	163.81	

Table 2
Average threshold mixing energy E_m in ThO₂, in the unit of eV.

T (K)	E_m^{Th}		E_m^O	
	Cooper	Zhou	Cooper	Zhou
100	58.27	94.61	39.89	35.91
500	55.60	91.83	39.33	34.00
1000	51.44	83.54	40.03	30.40
1500	42.94	73.59	36.36	29.20

climbing image nudged elastic band (CI-NEB) method [45,46] as implemented in the LAMMPS package. In this study, migration paths of four different point defects are considered, including Th and O vacancies and Th and O interstitials, denoted as V_{Th} , V_O , Th_i and O_i , respectively. To maintain charge neutrality, each simulation cell contains an FP, with the constituting vacancy and interstitial initially separated at a distance over 3 nm to minimize the Coulomb attraction between them. In the NEB calculation, diffusion paths that have been predicted in previous calculations [44,47] are considered. Specifically, we consider 1st nearest neighbor exchange along $\langle 110 \rangle$ for V_{Th} (Fig. 1(b)) and along $\langle 100 \rangle$ for V_O (Fig. 1(c)). For Th_i , the interstitialcy mechanism as shown in Fig. 1(d) is considered, where the octahedron interstitial Th will displace a nearby Th atom along $\langle 100 \rangle$ to form a new interstitial at the nearby octahedral site. For O_i , the interstitialcy mechanism as shown in Fig. 1(e) is considered, where the octahedron interstitial O will displace a

nearby O atom along $\langle 110 \rangle$ to form a new interstitial at the nearby octahedral site. The migration barriers of the direct interstitial mechanisms for Th_i and O_i are found unfavorably high by DFT [44], and we have confirmed the same trend using the Cooper potential. Accordingly, the interstitial mechanisms are not included in the results. As the constituting vacancy and interstitial of an FP are of opposite charges, the migration barriers are computed as a function of their separation distance. This is done by fixing one point defect (e.g., vacancy) while moving the other (e.g., interstitial) towards the fixed one. Since the vacancy is not represented as a real particle in the molecular dynamics model, its actual position cannot be accurately determined for the intermediate images along the diffusion path. In the case of vacancy diffusion, the vacancy position is linearly interpolated using its starting and ending positions in each diffusion step to estimate the vacancy-interstitial separation distance for data analysis.

Results

In this Section, the results from MD simulations are presented to elucidate how the threshold displacement energy depends on PKA type (i.e., cation v.s. anion), temperature, and orientation.

Dependence of E_d and E_m on PKA type

The results from the simulations at 1500 K are presented here to compare E_d of cation and anion. In Fig. 2(a) and (b), the probabilities of having an unchanged cell, defectless mixing, and defect formation are plotted versus the PKA energy for Th and O PKAs, respectively. Here, data obtained with all PKA directions are included to obtain the polar-averaged threshold energies over all crystal orientations. The results are listed in Table 1 and Table 2. Note that E_m should always be lower than E_d because displacing atoms from their original lattice sites is a prerequisite for defect formation. For Th PKA, DFP exceeds 50% at $E_d^{Th} = 61.21$ eV at 1500 K, much lower than that for O PKA, $E_d^O = 184.90$ eV, indicating that it's much harder to create FPs with O PKA. In contrast, it's easier to cause atomic displacement, which includes both defectless mixing and defect formation, with O PKA than with Th PKA. The corresponding average thresholds are $E_m^{Th} = 42.94$ eV and $E_m^O = 36.36$ eV, respectively. Similar trends have been reported by Dacus in UO₂, with $E_m^O < E_m^{Th}$ and $E_d^O > E_d^{Th}$ [21]. We have also recomputed E_d and E_m in UO₂

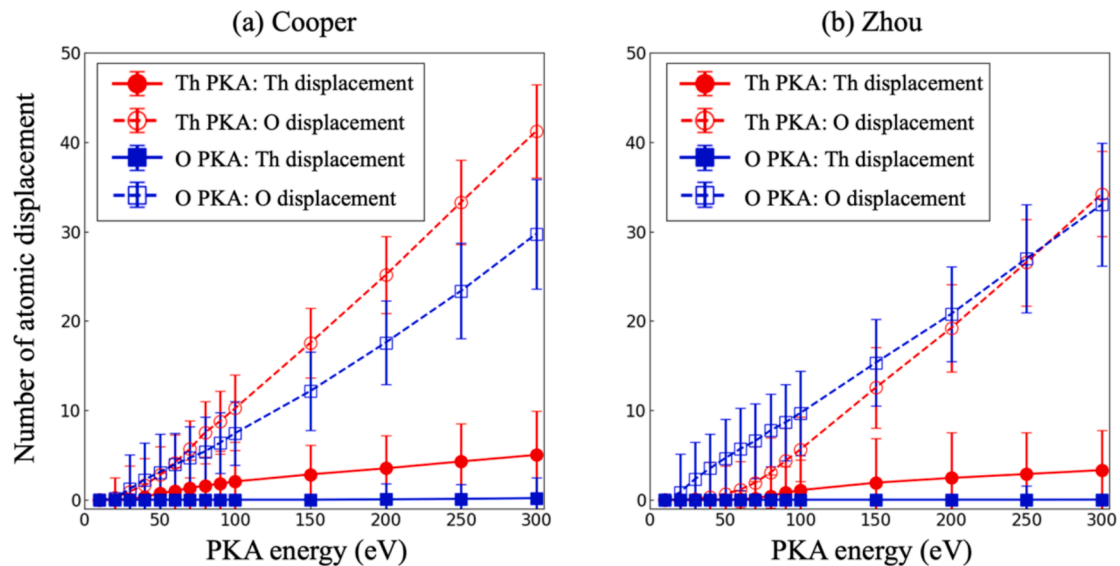


Fig. 3. Average numbers of Th (solid markers) and O (open markers) atoms versus PKA energy that are displaced by Th (red circles) and O (blue squares) PKAs obtained with (a) the Cooper and (b) the Zhou potential at 1500 K. The error bar indicates one standard deviation. (For interpretation of the references to colour in this figure legend, the reader is referred to the web version of this article.)

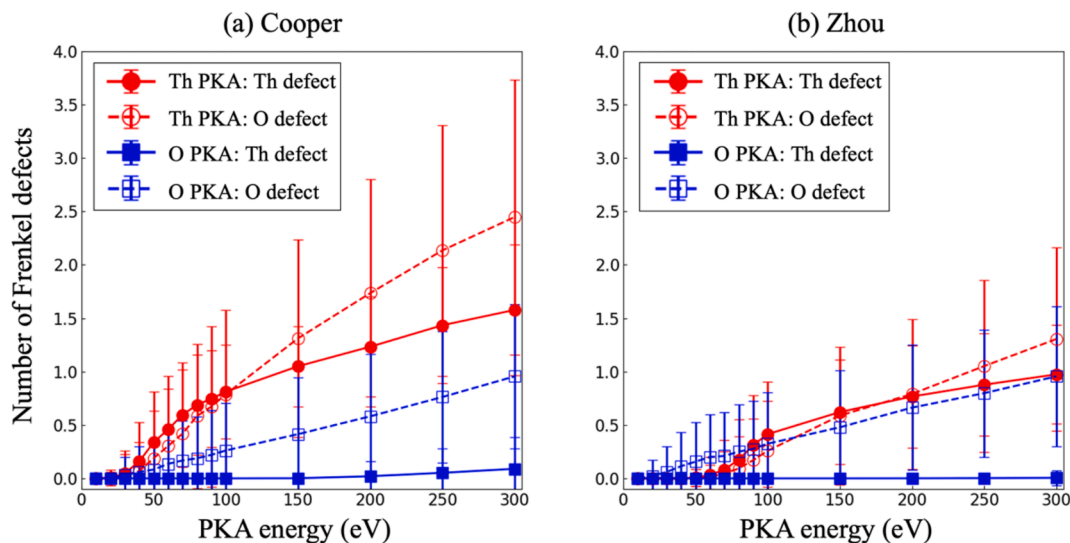


Fig. 4. Average numbers of stable Th (solid markers) and O (open markers) FPs versus PKA energy that are produced by Th (red circles) and O (blue squares) PKAs obtained with (a) the Cooper and (b) the Zhou potentials at 1500 K. The error bar indicates one standard deviation. (For interpretation of the references to colour in this figure legend, the reader is referred to the web version of this article.)

using the Cooper potential and received an excellent agreement with Dacus et al., as shown in Fig. S3 in the Supplementary Materials. The similar behaviors in ThO₂ and UO₂ suggest that there is possibly a general trend in fluorite-structured oxides that it's easier to cause atomic displacement but hard to form stable FPs with anion PKAs than with cation PKAs.

The different dependence of E_d and E_m on PKA type implies an important impact of defect recovery mediated by correlated recombination, which can be elucidated by the probability of defectless mixing. As shown in Fig. 2, the probability of defectless mixing for O PKA is much higher than for Th PKA, implying significantly more FPs resulting from the displaced atoms by O PKA recover via correlated recombination in thermal spike. This is consistent with a recent work in TiO₂, which shows that thermally-activated, correlated recombination in thermal spike leads to a strong temperature dependence of E_d^O [19]. Qualitatively, the Cooper and the Zhou potentials give the same dependence of E_d and E_m on PKA type, albeit some quantitative

differences in the exact values. In comparison, the Cooper potential gives higher E_d^O and E_m^O but lower E_d^{Th} and E_m^{Th} than the Zhou potential at 1500 K.

The results in ThO₂ from the current work and in UO₂ in Dacus et al. [21] (confirmed in this work as well) indicate that the average E_d for cation is lower than for anion in fluorite oxides. The opposite trend has been shown by Jiang et al. [16] in UO₂ and Xiao et al. [17] in ThO₂ using AIMD simulations and by Meis et al. [27] using static simulations with a different potential. This discrepancy may be resolved by examining whether E_d is computed based on DFP or ADP and whether correlated recombination in thermal spike is fully taken into consideration. According to Table 1, Xiao et al. [17] predicted a smaller E_d than Rahman et al. [26] and this work. The discrepancy may come from multiple reasons, including the definition of E_d adopted in post-processing, the interatomic potentials in MD, and the short simulation time in DFT. Meis and Chartier computed the threshold displacement energy using static calculations by displacing the PKA from its lattice site without dynamic

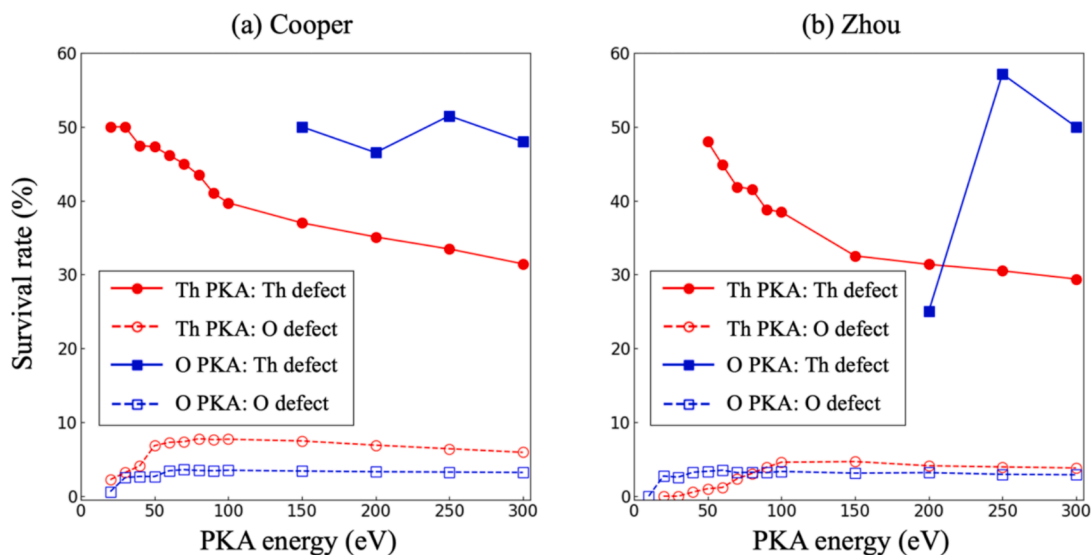


Fig. 5. Survival rates of Th (solid markers) and O (open markers) FPs versus PKA energy that are produced by Th (red circles) and O (blue squares) PKAs obtained with (a) the Cooper and (b) the Zhou potential at 1500 K. (For interpretation of the references to colour in this figure legend, the reader is referred to the web version of this article.)

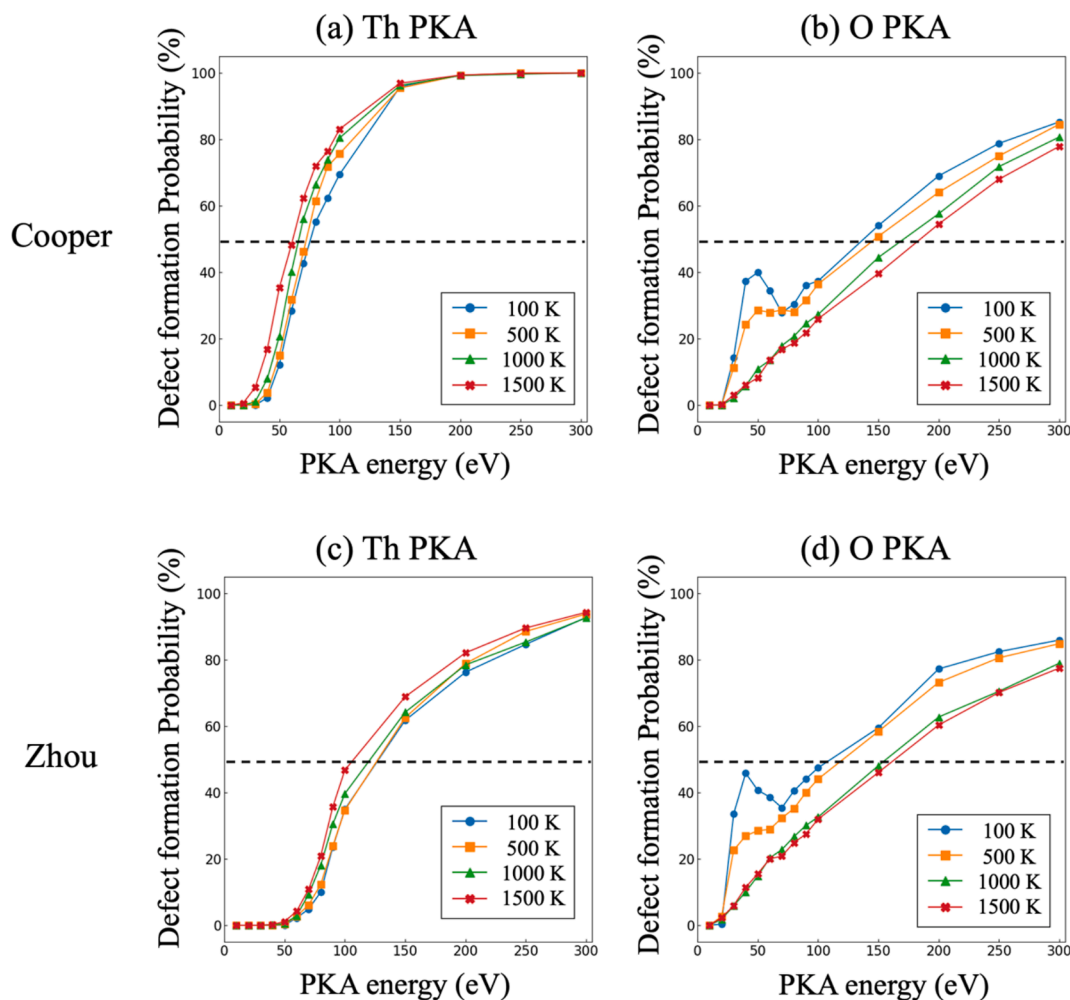


Fig. 6. Defect formation probability at 100 K, 500 K, 1000 K, and 1500 K as a function of PKA energy for (a) Th PKA and (b) O PKA with the Cooper potential, and (c) Th PKA and (d) O PKA with the Zhou potential.

relaxation, ignoring correlated recombination in thermal spikes. The resulting threshold is based on ADP and corresponds to E_m in this work. In Jiang et al. and Xiao et al., the threshold displacement energy is obtained with the criterion of whether the PKA is permanently displaced from its lattice site without explicitly confirming FP formation from the whole system. Also, as pointed out by Robinson et al. [19], the 1 ps simulation duration may suppress correlated recombination and underestimate E_d . Further, due to the high computation cost, only one AIMD simulation is carried out for each PKA energy along each orientation. The lack of statistics could have affected the average E_d since primary defect production is highly stochastic. This comparison highlights the importance of adopting the relevant definition and a standard calculation procedure to ensure a valid comparison of results from different studies.

To clarify the different impacts of correlated recombination on E_d^{Th} and E_d^O , the types of displaced atoms and FPs are analyzed. In Fig. 3, the average numbers of displaced Th and O atoms are plotted versus PKA energy. At the beginning of each simulation, Wigner-Seitz analysis is carried out with each atom located at the center of its own Wigner cell. The number of displaced atoms is obtained as the number of atoms that are not in their original Wigner cells at the end of the simulation. This may underestimate the number of displaced atoms because some may return to their original cells during recovery. The results obtained with the Cooper potential are shown in Fig. 3(a) and the Zhou potential in Fig. 3(b). Th PKAs displace both Th and O atoms, and significantly more O atoms than Th are displaced. In contrast, O PKAs mostly displace O

atoms with negligible Th displacement. This might be related to a much smaller mass of O than Th, making it hard to transfer kinetic energy from O to Th. Qualitatively, similar trends are observed with both potentials.

Both Th and O FPs are produced with Th PKAs when PKA energy is larger than 30 eV with the Cooper potential (Fig. 4(a)) and 60 eV with the Zhou potential (Fig. 4(b)). In contrast, primarily only O FPs are produced by O PKAs. With the same kinetic energy, Th PKAs generate more O FPs than O PKAs; this is true for all PKA energies with the Cooper potential (Fig. 4(a)) and for PKA energy > 100 eV with the Zhou potential. The numbers of stable FPs are significantly lower than that of displaced atoms, particularly for O FPs, indicating the importance of correlated recombination in thermal spikes.

To quantify the impact of correlated recombination, the survival rate is introduced and defined as the ratio of stable FPs formed over the number of atoms displaced. Note the survival rates may be overestimated because the number of displaced atoms is possibly underestimated. As shown in Fig. 5(a) and (b), no matter produced by Th or O PKAs, displaced Th atoms have much higher survival rates than displaced O atoms. At 1500 K, the O survival rate is less than 10% for both Th PKA and O PKA, indicating that more than 90% of displaced O atoms recover via recombination, leaving no FPs. In comparison, the Th survival rate is approximately 30%–50%. It is important to note that the Th survival rate computed with O PKAs may be inaccurate because O PKAs rarely displace Th atoms. This confirms that correlated recombination leads to a more significant recovery of displaced O atoms. Also, since O PKAs generate O FPs almost exclusively with rare Th displacements,

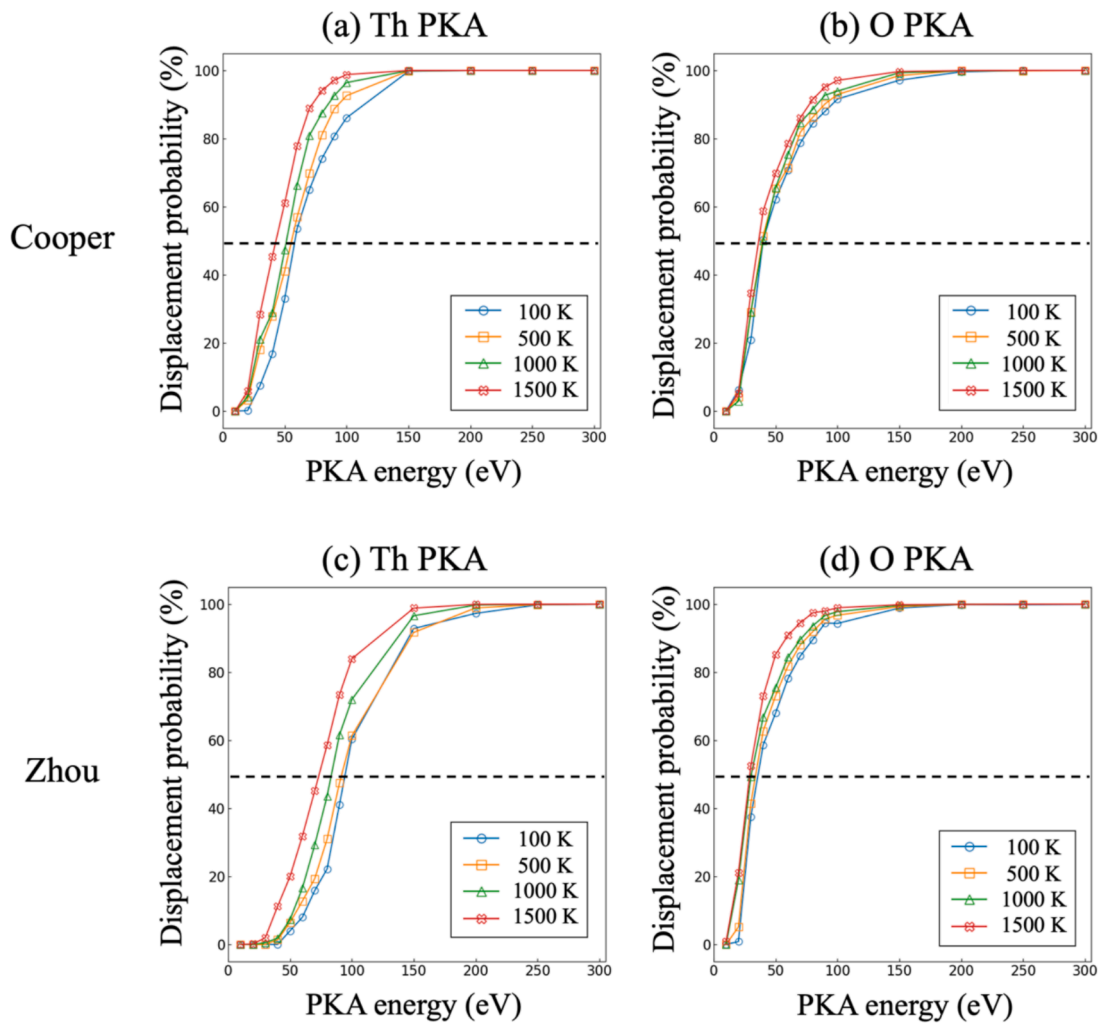


Fig. 7. Atomic displacement probability at 100 K, 500 K, 1000 K, and 1500 K as a function of PKA energy for (a) Th PKA and (b) O PKA with the Cooper potential, and (c) Th PKA and (d) O PKA with the Zhou potential.

correlated recombination can significantly affect FP production and lead to a large difference between E_m^O and E_d^O , i.e., much lower $E_m^O = 36.36$ eV than $E_d^O = 184.90$ eV at 1500 K. While for Th PKA, the survival rate of Th is relatively high (>30 %), meaning a smaller difference between E_m^{Th} (42.94 eV) and E_d^{Th} (62.21 eV) because of less significant recombination

of displaced Th atoms.

Also, Fig. 5 shows that O atoms displaced by Th PKAs have higher survival rates than O atoms displaced by O PKAs. Similarly, displaced Th atoms by O PKAs have higher survival rates than those displaced by Th PKAs. When atoms are displaced by an opposite type of PKA, both Th

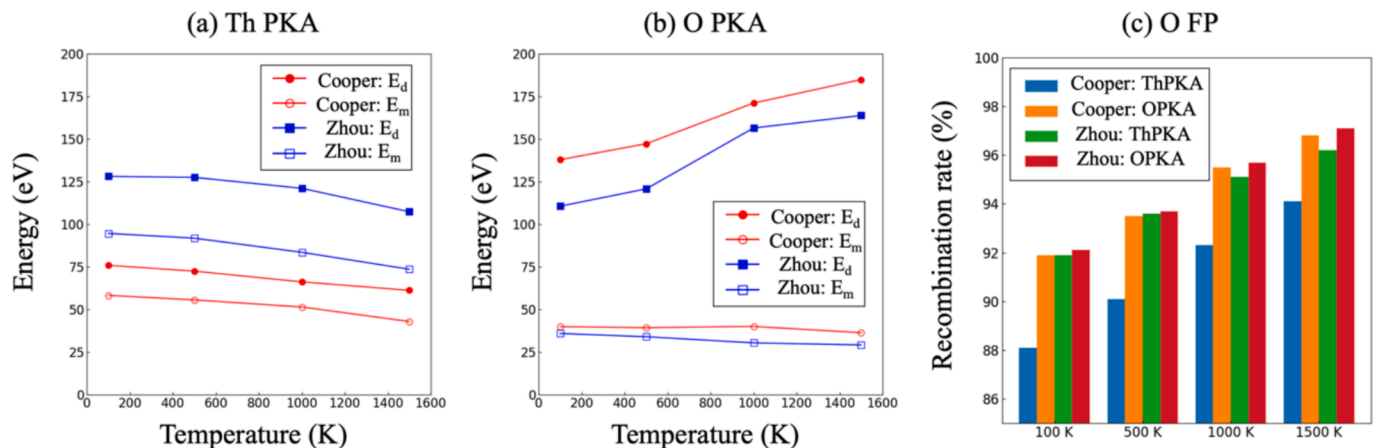


Fig. 8. Threshold displacement energy and threshold mixing energy as a function of temperature for (a) Th PKA and (b) O PKA for Cooper potential and Zhou potential. In (c), fractions of recombined O FPs generated by 300 eV Th and O PKAs are shown versus temperature.

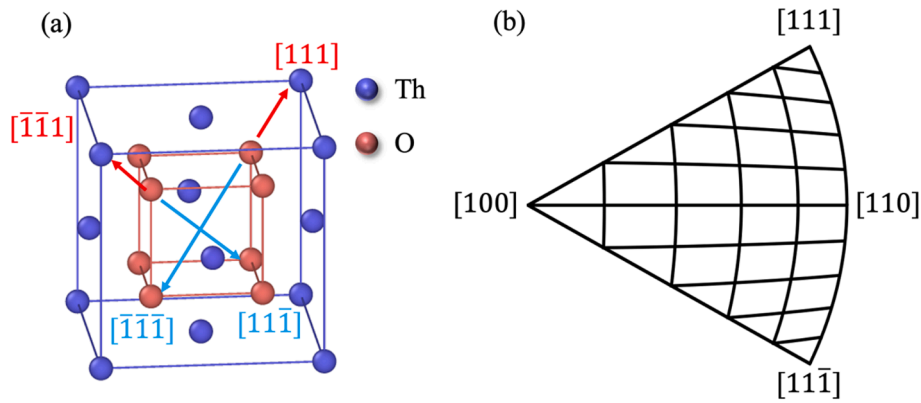


Fig. 9. (a) A fluorite ThO_2 conventional cell showing the asymmetry of $[111]$ and $[\bar{1}\bar{1}\bar{1}]$ for the selected O atom. Note that $[111]$ is equivalent to $[\bar{1}\bar{1}\bar{1}]$ and $[\bar{1}\bar{1}\bar{1}]$ is equivalent to $[111]$. (b) A schematic view of stereographic projection with 30 direction groups to fully consider the orientation dependence of E_d^{O} .

and O FPs are generated and they co-exist. In Fig. S4 in the Supplementary Materials, the probabilities of generating i) Th FPs only, ii) O FPs only, and iii) Th + O FPs are plotted versus PKA energy. As expected, O PKAs mostly generate O FPs only without Th FPs. With low PKA energy, Th PKAs have similar probabilities for generating Th FPs only and Th + O FPs. While with high PKA energy, it's much more likely for Th PKAs to generate both Th + O defects than Th FP only. We further computed the survival rates of displaced Th and O atoms with and without their co-existence. The results are plotted in Fig. S5 in the Supplementary Materials. It's shown that in the high PKA energy range, the survival rate is higher for both Th and O FPs when they co-exist for the Cooper potential. Therefore, the coexistence of Th and O FPs may reduce correlated recombination.

As a summary of the above analysis, although O PKA shows a lower threshold mixing energy than Th PKA, it features a much higher threshold displacement energy E_d^{O} because of its exclusive production of O FPs which are subjected to significant correlated recombination. However, the reason behind the more significant recombination of O FPs is unclear, which will be further discussed in the Discussion section.

Temperature dependence of E_d and E_m

Following the same procedure as in Fig. 2, ADPs and DFPs are computed at 100 K, 500 K, and 1000 K as well. For all temperatures, the DFPs are plotted against PKA energy in Fig. 6 and ADPs in Fig. 7. The results for average E_d are listed in Table 1 along with data from the literature, and for average E_m in Table 2. As shown in Fig. 6(a) and (c), the DFP curve for Th PKA shifts to the left with increasing temperature, indicating decreasing E_d^{Th} , while the DFP curve for O PKA in Fig. 6(b) and (d) shifts to the right, indicating increasing E_d^{O} . Differently, the ADP curves for both Th and O PKAs in Fig. 7 shift to the left, meaning that both E_m^{Th} and E_m^{O} decrease with increasing temperature. Relatively, E_d^{Th} (see Fig. 7(a) and (c)) has a stronger temperature dependence than E_m^{O} (see Fig. 7(b) and (d)). The same trends are obtained with both the Cooper and the Zhou potential. The results suggest that increasing temperature makes it easier to displace atoms from their original sites but not necessarily give more primary defect production.

To better show the temperature dependence, both E_m and E_d are plotted in Fig. 8 versus temperature. For Th PKA, both E_m^{Th} and E_d^{Th} decrease monotonically with temperature, as shown in Fig. 8(a). The common temperature dependence shared by E_m^{Th} and E_d^{Th} implies that correlated recombination may not affect defect production with Th PKA as significantly as with O PKA. The decrease in E_m^{Th} and E_d^{Th} with increasing temperature can be explained by weakening interatomic interactions caused by increasing temperatures, similar to the case that has been observed in metals [15,25]. Comparing the potentials, the Cooper

potential gives lower E_m^{Th} and E_d^{Th} than the Zhou potential. For O PKA, E_m^{O} shows a weaker dependence on temperature with a slight decrease, while E_d^{O} increases clearly with temperature. The Cooper and the Zhou potential share the same trends, while the former gives higher E_m^{O} and E_d^{O} than the latter. The opposite temperature dependence of E_m^{O} and E_d^{O} can again be explained by correlated recombination. The temperature dependence of E_d obtained in the present work is consistent with that in Rahman et al. [26] To elucidate this point, the fraction of recombined O FPs generated by 300 eV Th and O PKAs are plotted versus temperature in Fig. 8(c). Here, the recombination rate equals one minus the survival rate shown in Fig. 5. There is a clear increase in the fraction of recombined O FPs with temperature, showing temperature facilitates their correlated recombination. Because of this, E_d^{O} increases with temperature, also E_m^{O} is nearly constant. The increasing recombination rate with temperature indicates that correlated recombination may be thermally activated. As has been shown by Brutzel et al. [48], in UO_2 FP with a separation distance over 7 Å recombine by thermally activated diffusion with a barrier smaller than the regular diffusion barrier.

The impact of correlated recombination on defect production by O PKA is also indicated by the observation of an unexpected peak in the DFP curves for O PKA shown in Fig. 6(b) and (d). At 100 K, a peak is observed around 40–50 eV for both the Cooper and the Zhou potential. This peak weakens at 500 K and vanishes at 1000 K and 1500 K. Such a peak has not been reported in fluorite oxides in the literature and can be explained by the effect of correlated recombination. It is interesting to notice that the peak is located close to the threshold mixing energy for O PKA, E_m^{O} , 39.89 eV predicted by the Cooper and 35.91 eV by Zhou at 100 K, as shown in Table 2. As the PKA energy exceeds E_m^{O} , the excess energy, which is the difference between the PKA energy and that is used to generate atomic displacements, will be dissipated as heat to raise the local temperature in the thermal spike. Increasing the PKA energy right above E_m^{O} and thereby the excess energy will increase the thermal spike temperature and enhance correlated recombination, resulting in fewer stable FPs and a lower DFP. This effect is important at low temperatures that are insufficient to activate significant recombination. As temperature increases, the impact of thermal spike temperature becomes less important relatively. Accordingly, the peak weakens gradually and vanishes at high temperatures. Compared to O PKA, this peak is not observed for Th PKA, again implying that defect production by Th PKA is not affected by correlated recombination as significantly as for O PKA.

Orientation dependence of E_d and E_m

A detailed analysis of the orientation dependence of E_d and E_m is presented using stereographic projection considering crystal symmetry. Both the fcc cation and the simple cubic (sc) anion sub-lattices in the

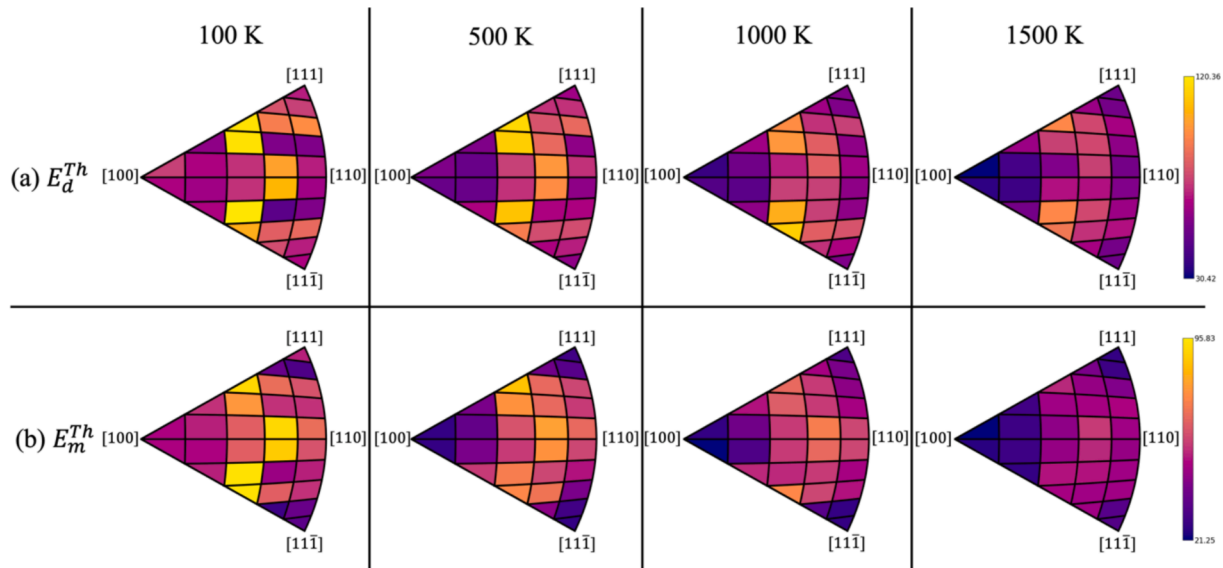


Fig. 10. Map of threshold displacement energy E_d (top row) and threshold mixing energy E_m (bottom row) obtained with the Cooper potential at 100 K, 500 K, 1000 K, and 1500 K for Th PKA. Both E_d and E_m are in unit of eV.

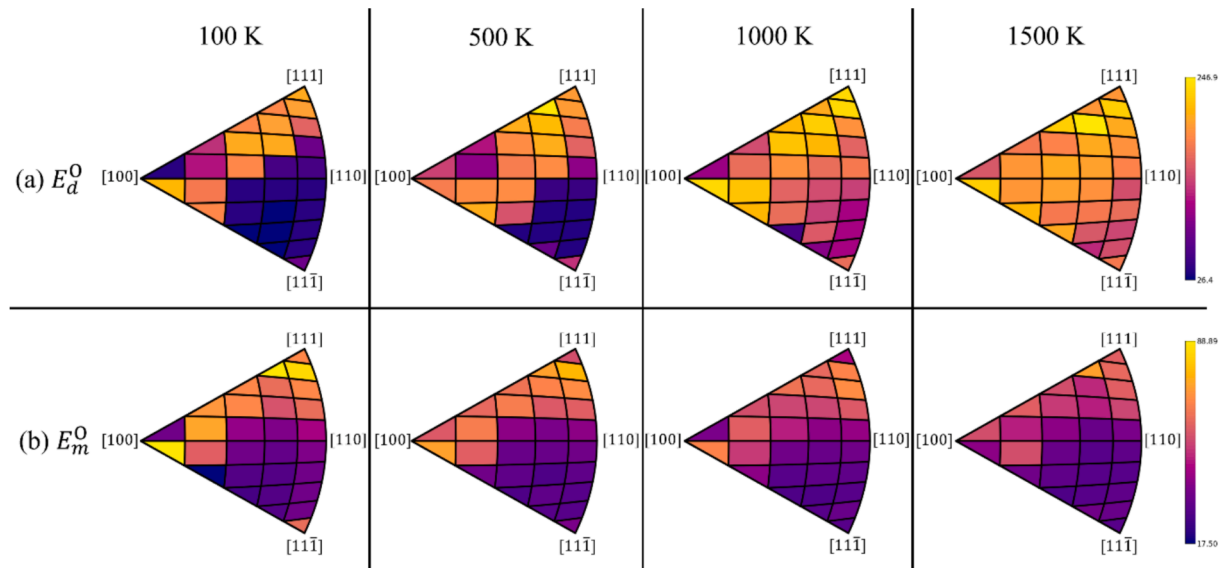


Fig. 11. Map of threshold displacement energy E_d (top row) and threshold mixing energy E_m (bottom row) obtained with the Cooper potential at 100 K, 500 K, 1000 K, and 1500 K for O PKA. Both E_d and E_m are in the unit of eV.

fluorite structure follow cubic symmetry. In cubic systems, the $\langle 100 \rangle - \langle 110 \rangle - \langle 111 \rangle$ stereographic projection triangle is sufficient to represent all equivalent crystal orientations. As a result, low-index orientations such as $\langle 100 \rangle$, $\langle 110 \rangle$ and $\langle 111 \rangle$ are often used to study the displacement threshold energy in UO_2 and ThO_2 . However, a hidden asymmetry arises from the coexistence of the fcc and sc sublattices. As illustrated in Fig. 9 (a), the selected O atom reveals an asymmetry along $[111]$ and $[\bar{1}\bar{1}\bar{1}]$, facing a Th atom along the former and an O atom along the latter. To accurately account for the orientation dependence of E_d^O , a broader stereographic zone incorporating both the $\langle 100 \rangle - \langle 110 \rangle - \langle 111 \rangle$ and the $\langle 100 \rangle - \langle 110 \rangle - \langle 11\bar{1} \rangle$ triangles is necessary, as shown in Fig. 9(b). This asymmetry does not exist for Th atoms. Still, the stereographic projection shown in Fig. 9(b) is used for Th PKAs to demonstrate the different symmetry. In the stereographic projection, all PKA directions are divided into 30 groups. With 2000 PKAs considered for each combination of PKA energy and temperature, each group contains

approximately 67 PKAs on average. For each group, a single polar-averaged E_d and E_m are computed based on the DFP and ADP curves using the data from PKAs within each orientation group. However, the limited number of PKAs in each group is insufficient to estimate the uncertainty using the method described in Section S4 of [Supplementary Materials](#). In comparison, the results in [Tables 1 and 2](#) presented in the previous subsections are averaged over PKAs in all directions, i.e., averaged over all orientation groups.

In [Figs. 10 and 11](#), E_d and E_m obtained with the Cooper potential at different temperatures are mapped into different orientation groups for Th and O PKAs, respectively. The corresponding results obtained with the Zhou potential are presented in [Figs. S6 and S7](#) in the [Supplementary Materials](#). Albeit the stochastic uncertainty caused by the relatively small number of PKAs in each group, clear orientation dependence can be observed. For Th, the $\langle 100 \rangle - \langle 110 \rangle - \langle 111 \rangle$ and the $\langle 100 \rangle - \langle 110 \rangle - \langle 11\bar{1} \rangle$ triangles mirror each other, showing that the cubic symmetry is

Table 3

Frenkel defect formation energies and the ratio of E_m and E_d over E_{FP} obtained in this work and from the literature, in the unit of eV.

	E_{FP}^{Th}	E_m^{Th}/E_{FP}^{Th}	E_d^{Th}/E_{FP}^{Th}	E_{FP}^O	E_m^O/E_{FP}^O	E_d^O/E_{FP}^O
Cooper potential	14.27	4.08	5.32	5.08	5.32	27.14
Zhou potential	20.89	4.53	6.13	4.95	6.13	22.34
DFT	12.57[49]			4.03[49]		
	15.59[44]			5.09[44]		
	16.72[50]			6.83[50]		
	13.71[51]			4.98[51]		
MD	17.50[52]			5.80[52]		
UO ₂	11.2[53]			3.3[53]		
	9.1–10.9			2.4–2.6		
	[54]			[54]		
				3.83[55]		
				4.2[56]		

preserved. Compared to the AIMD results in Xiao et al., which has $\langle 110 \rangle < \langle 100 \rangle < \langle 111 \rangle$ for E_d^{Th} , $\langle 100 \rangle$ seems to have the lowest E_d^{Th} . The highest E_m^{Th} and E_d^{Th} are found not located at low-index orientations. It is needed to have a full orientation study. Again we note that there are no statistics in the AIMD study and the results are subject to large stochastic uncertainty. With increasing temperature, E_m^{Th} decreases in all orientation groups, and so does E_d^{Th} , probably due to weakening atomic bonding.

For O PKA, a clear asymmetry can be seen by comparing the $\langle 100 \rangle - \langle 110 \rangle - \langle 111 \rangle$ with the $\langle 100 \rangle - \langle 110 \rangle - \langle 11\bar{1} \rangle$ triangle. For both E_m^O and E_d^O , lower values are obtained in the $\langle 100 \rangle - \langle 110 \rangle - \langle 11\bar{1} \rangle$ triangle than in the $\langle 100 \rangle - \langle 110 \rangle - \langle 111 \rangle$ triangle, indicating that it is easier to cause atomic displacement and defect production with O PKAs displaced towards 1st O neighbors along the $[111]$ direction (see Fig. 9(a)). This asymmetry weakens but is still visible at 1500 K, particularly for E_m^O , as shown in Fig. 11. For E_d^O , the orientation dependence is much weaker at 1500 K than at 100 K. This may be caused by enhanced correlated recombination at 1500 K. The recombination does not have a strong orientation dependence, with a trend to make E_d isotropic.

While by average $E_d^O > E_m^O$ at all temperatures, it is interesting to notice that at low temperatures, the minimum E_d^O (~ 26.4 eV in Fig. 10 (a)) is actually below the minimum E_m^O (~ 30.42 eV in Fig. 11(a)). In experiments where E_d is based only on detectable defects, the measured E_d is likely the lower bound rather than the average. Moreover, the high-energy irradiation (keV to MeV) generates a higher number of O defects than Th defects, which agrees with Fig. 4. Our result also suggests the KP model, which estimates E_d based on the number of defects results on lower E_d^O than E_m^O when PKA energy is higher than 200 eV. Therefore, likely a lower E_d^O will be measured than E_m^O in such experiments, as has been done in UO₂[30].

Discussions

In the Results section, it has been shown that O FPs are subjected to more significant correlated recombination in thermal spike than Th FPs. However, the reason behind this is unclear. In this section, defect formation energies and migration barriers are computed to understand the reason and elucidate which factor governs recombination in the thermal spike. An effect of the Coulomb interaction between charged defects on both the formation energy and migration barrier of point defects, as well as on correlated recombination, is identified. Some limitations of the present study are discussed as well.

Frenkel pair formation energies and point defect migration barriers

To avoid Coulomb interaction between periodic cells, charge neutrality needs to be maintained in MD simulations. A single type of

Table 4

NEB-calculated migration energy (eV) of point defects in ThO₂ in comparison with previous DFT research.

	V _{Th}	Th _I	V _O	O _I
Cooper	4.67	3.71	0.53	1.57
Zhou	5.65	1.99	0.41	1.01
Reference of	5.63 (DFT	4.15 (DFT	0.537(MD[63])	1.17 (DFT[44])
ThO ₂	[44])	[44])	0.81 (DFT[44])	0.13–1.04 (DFT
	6.67 (DFT		1.97–3.36 (DFT	[47])
	[60])		[64])	0.92 (DFT[62])
	4.47 (DFT		2.16–3.34 (DFT	
	[61])		[65])	
	7.04 (DFT		1.27 (DFT[61])	
	[62])		0.78 (DFT[62])	
Reference of	4.8 (DFT	3.7 (DFT	1.34–2.46(DFT	0.69–1.35(MD
UO ₂	[53])	[53])	[64])	[66])
	3.8(MD	2.1–3.1(MD	0.34–0.44(MD	
	[66])	[66])	[66])	

point defects, e.g., V_{Th} or V_O, cannot form independently while adhering to charge neutrality, rather, they form in the form of Schottky defects or Frenkel pairs (FPs). Here, we focus on the FP formation energies because they are more relevant to primary defect production. The results are listed in Table 3, along with the data from the literature. The results obtained with the Cooper potential agree well with previous DFT calculations by Jiang et al. on both E_{FP}^{Th} , 14.27 eV versus 15.59 eV, and E_{FP}^O , 5.08 eV versus 5.09 eV, and are within the ranges of previous DFT results, 12.57 eV to 16.72 eV for Th FP and 4.03 to 6.83 for O FP, as shown in Table 3. The Zhou potential predicts a higher E_{FP}^{Th} (20.89) than DFT calculations. The predicted E_{FP}^O (4.95) is also within the range of DFT results.

Previously, the FP formation energy E_{FP} has been related to threshold displacement energy E_d . For instance, Kittiratanawasin et al.[57] suggest that E_d correlates positively with and is about 4–10 times of E_{FP} . The study in Y₂Ti₂O₇[58] also suggests that E_d correlates positively with E_{FP} . To examine this correlation, we have computed the ratios of E_m and E_d over E_{FP} . The results are listed in Table 3. As can be seen, the positive correlation holds between E_m and E_{FP} for both Th and O FPs. O FP has a lower formation energy than Th PKA, and accordingly, the threshold mixing energy is lower for O than for Th PKAs. The ratio E_m^{Th}/E_{FP}^{Th} is 4.08 with the Cooper potential and 4.53 with the Zhou potential, and the ratio E_m^O/E_{FP}^O is 5.32 with the Cooper potential and 6.13 with the Zhou potential. The correlation seems to hold for E_d^{Th}/E_{FP}^{Th} as well, possibly because Th FPs are less affected by correlated recombination. However, the correlation seems invalid for E_d^O/E_{FP}^O , which is found to be above 20 with both potentials. This implies that the FP formation energy may correlate more closely with the threshold mixing energy for displacing atoms, E_m , than with the threshold displacement energy for generating stable FPs, E_d , particularly when correlated recombination is significant.

It should also be noted that once an FP has been created, the formation energy serves as the thermodynamic driving force for recombination. The higher formation energy of Th FP means that Th FP has a higher driving force to recombine than O FP, which is the opposite of the trend in the recombination rates shown in Fig. 5. This suggests that correlated recombination in thermal spike is not governed by thermodynamics but more likely by kinetics.

The very different migration barriers of Th and O defects provide a plausible explanation for why O FPs are subjected to more significant recombination than Th FPs in thermal spike. Similar to UO₂[21,59], the highly mobile oxygen ions exhibit fast defect recovery and a short lifetime. In Table 4, the barriers for V_{Th}, V_O, Th_I, and O_I computed by NEB are listed along with the literature data. For V_{Th}, the calculated barriers of 4.67 eV (Cooper) and 5.65 eV (Zhou) are within the DFT results, which vary from 4.47 eV to 7.04 eV, as shown in Table 4. For Th_I, the values of 3.71 eV (Cooper) and 1.99 eV (Zhou) are lower than the only DFT result of 4.15 eV from Jiang et al.[44]. For V_O, the computer barrier

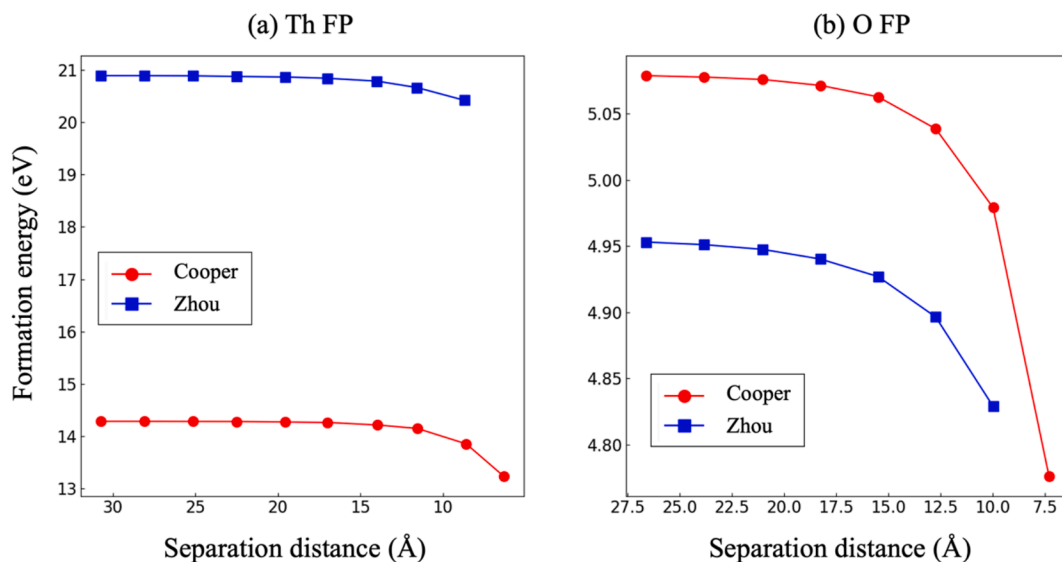


Fig. 12. Formation energies of (a) Th Frenkel pair and (b) O Frenkel pair as a function of separation distance.

of 0.53 eV (Cooper) and 0.41 eV (Zhou) is lower than the DFT values, which vary from 0.537 eV to 3.36 eV, as shown in Table 4. For O_I , the barrier of 1.57 eV from the Cooper potential is above, and that of 1.01 eV from the Zhou potential is within the DFT range of 0.13 eV to 1.17 eV. While both potentials agree reasonably well with DFT calculations, their results on point defect migration barriers in reference to DFT are mixed without a clear conclusion. The large variations in the DFT results also make it hard to select a reliable reference for assessing the performance of empirical potentials.

For the relatively low PKA energies studied, no melting occurs in the thermal spike, which is different than the case of displacement cascades generated by high-energy PKAs. In the low PKA energy range, correlated recombination is likely mediated by thermally activated migration of point defects, as suggested by the temperature dependence observed in TiO_2 [19] and ThO_2 in this work (see Fig. 8(c)). The defect migration may be further facilitated by the high local temperature and the distortion of local crystal structure in thermal spike. Because the migration barriers of V_{Th} and Th_I are both high (the lowest is the Th_I barrier predicted by the Zhou potential, 1.99 eV), migration of Th defects is limited in the short thermal spike lifetime, which is in the order of a few ps. In comparison, migration of O defects involves much lower barriers. With both the Cooper and the Zhou potential, V_O has a much lower barrier than O_I , meaning that correlated recombination is likely dominated by diffusion of V_O . The very low barrier of V_O suggests that significant recombination can occur at high temperatures. Even at low temperatures, recombination can still occur because of the elevated temperature in the thermal spike, as suggested by the unexpected peaks in the DFPs curves in Fig. 6(b) and (d).

Effect of Coulomb interaction

The Coulomb interaction between charged defects may also facilitate correlated recombination, particularly for O FPs. Unlike in metals, where point defects have no charges and their formation is not constrained by stoichiometry, point defects in oxides are charged. While described by fixed charge interatomic potentials such as the Cooper and Zhou potentials, the charges of interstitials are given by the ions constituting the interstitials, and that of vacancies are by the opposite of the displaced ions. Accordingly, Th_I and V_O are positively charged, and O_I and V_{Th} are negatively charged. As such, the Coulomb interaction between the charged defects separated by short distances can affect both the thermodynamics (e.g., formation energy) and the kinetics (e.g., migration barrier) of point defects. For example, in metals, atoms

around a vacancy usually relax towards the vacant site. In contrast, in ThO_2 , relaxations around the defects are affected by their charges. Because of Coulomb interaction, ions having the same signs of charge with the defects will be repelled and move away from the defects, while those having the opposite signs will do the opposite. The relaxed defect configurations are shown in Fig. S9 in the Supplementary Materials. As shown in Fig. S9(a), O ions (Th ions) are repelled (attracted) by and relaxed away from (towards) V_{Th} because they are both negatively charged. The same is true for the case of O_I in Fig. S9(b). For the positively charged Th_I (Fig. S9(c)) and V_O (Fig. S9(d)), positively charged Th ions are repelled, and negatively charged O ions are attracted. In the literature, previous DFT results in ThO_2 have demonstrated that the magnitude of defect charge directly influences the relaxation volume and defect formation energy[67]. At low fermi levels, the formation energies of positively charged defects decrease with their charge, while those of negatively charged ones increase with the charge in ThO_2 . [51,67] The charge state can also influence the migration behavior of oxygen interstitials[47].

To explore the impact of Coulomb interaction between charged defects, both the FP formation energy and the point defect migration barrier are computed as functions of the FP separation distance. We start from the minimum distance at which an FP is stable against spontaneous recombination and increase the distance to about 3.0 nm, at which both the formation energy and migration barrier plateau. With the PKA energies considered, most FP separation distances are below 3.0 nm, except for 300 eV, for which the FP separation has been found to reach 3.5 to 4.0 nm, as shown by the histograms in Fig. S10 in the Supplementary Materials, where the distributions of FP separation distances obtained with 300 eV PKAs at 100 K and 1500 K are shown. The formation energies of Th and O FPs are plotted in Fig. 12. As the FP separation distance decreases, the corresponding formation energy decreases monotonically with both interatomic potentials. Across the separation distance, the formation energy of Th FP changes by about 0.47 eV with the Zhou potential and about 1.05 eV with the Cooper potential, and that of O FP changes by about 0.13 eV and 0.30 eV, respectively, as shown in Fig. 12.

The defect migration barrier also depends on the FP separation distance. Further, the barriers for the constituting defects in an FP to move towards and away from each other become asymmetrical. Accordingly, we define the forward (backward) barrier as the barrier for them to move towards (away from) each other. All barriers are presented in Fig. 13. The corresponding change in the total potential energy of the simulation cell along the migration path is shown in Fig. S11 for the

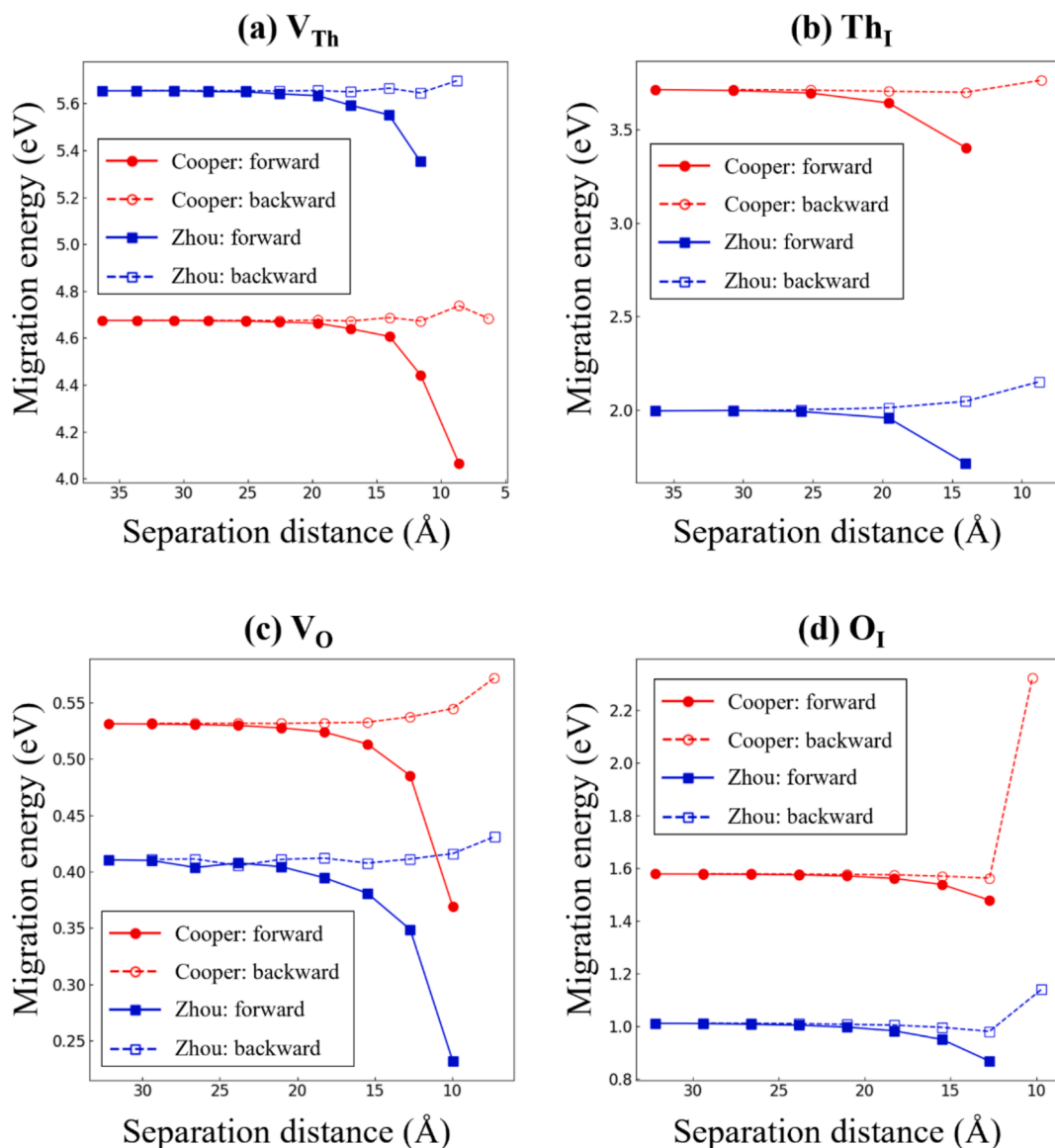


Fig. 13. Forward and backward migration barriers for (a) Th vacancy, (b) Th interstitial, (c) O vacancy, and (d) O interstitial as a function of Frenkel defect separation distance.

Cooper potential and the Zhou potential. As shown in Fig. 13, when the distance is beyond 2.5 nm, the forward barriers of all defects match the backward barriers, and both are independent of FP separation distance, meaning that the Coulomb interaction has a negligible effect. While below 2.5 nm, the forward and backward barriers start to diverge from each other, with higher backward than forward barriers. For all types of defects, the forward barriers decrease, and the backward barriers increase as the FP separation distance decreases. This dependence is attributed to the Coulomb interaction between the vacancies and interstitials forming the FPs. Because of their opposite charges, they attract each other. As shown in Fig. S11, both the saddle point energy and the local energy minima decrease (increase) when they move towards (away from) each other. The resulting distance-dependent migration barrier will facilitate correlated recombination in two ways. First, it leads to lower barriers for recombination with a smaller FP separation distance. This explains the lower barriers for FP recombination at small distances than the regular thermal diffusion barrier observed in UO_2 [48]. Second, because of the asymmetry of forward and backward barriers, the thermally activated random-walk diffusion will be biased. The defects will have higher probabilities of moving towards

than away from each other. As the asymmetry starts at about 2.5 nm, the Coulomb interaction between charged defects may affect uncorrelated recombination during long-term defect evolution as well.

Limitations

The present study utilizes classical MD simulations, which are less accurate than AIMD in terms of describing the interaction between ions. However, the much better computation efficiency allows using much larger simulation cells, longer relaxation time, and much better statistics than in AIMD simulations. Therefore, compared to AIMD, classical MD can minimize the self-interaction of defects because of small simulation cell size, fully consider correlated recombination, and minimize stochastic uncertainty. Still, cautions are needed, bearing in mind the empirical nature of the interatomic potentials adopted. The results obtained with the two potentials agree well with each other on the general trends for the dependence of E_d on PKA type, temperature, and orientation. The quantitative differences between the results from these two potentials imply the challenge of obtaining quantitative threshold displacement energy. Comparing these two potentials, the predicted FP

formation energy and defect migration barriers by the Cooper potential agree well with recent DFT calculations in Jiang et al. [44], suggesting its suitability for simulating defect behavior. The development of Zhou's potential focuses more on the phonon properties in a perfect crystal [33].

The adoption of fixed-charge potentials may limit the investigation of the effect of defect charge. Because each ion carries a fixed charge, each point defect has a fixed effective charge as well, with the values prescribed by the potentials. The actual charges of defects in ThO₂ have not been fully determined. The possibility exists that the charges of the defects differ from those of the ions in two ways. First, the ions may have flexible valence and adopt different charge states in the defected structures than in perfect crystals. For example, in an AIMD study, Xiao et al. [47] suggested that charge redistribution causes the delocalization of electrons on neighboring atoms for O vacancy. As another example, U ions in UO₂ can adopt different charge states [54,56,68]. In comparison, Th ion is less flexible in terms of charge state, and ThO₂ exists mostly as a hypo-stoichiometric oxide [51,67]. Second, radiation may generate F-centers [69–73], especially for O defects. Unlike point defects which are hard to detect, F-centers can be visualized by optical imaging and Raman spectroscopy, providing valuable insights into the material's electronic structure and response to radiation [69,74]. The existence of F-centers has been confirmed and can cause a dramatic decrease in thermal conductivity in KCl, KBr, KI, and NaF [75]. In ThO₂, Dennett et al. suggest that the F-center may have a significant impact on thermal conductivity due to resonant scattering [70]. A full understanding of the primary defects will need the fractions of all types of defects produced, which may require an efficient methodology that is capable of describing flexible valence and decoupled electrons.

Conclusions

This work presents a comprehensive investigation of threshold displacement energy, E_d , to elucidate its dependence on PKA type, orientation, and temperature in ThO₂ using classical molecular dynamics simulations. The results show the critical importance of distinguishing two different thresholds: the threshold for displacing atoms from the lattice site, denoted as E_m , and the threshold for generating stable FPs, denoted as E_d . The below conclusions are drawn from the findings:

- While E_m is lower for O PKA (E_m^O) than for Th PKA (E_m^{Th}), a higher average E_d^O is needed to create stable FPs with O PKAs than with Th PKAs, E_d^{Th} . This is because of the more significant correlated recombination of O FPs in thermal spike due to the much lower migration barriers of O defects than Th defects. The common trends shared by ThO₂ and UO₂ suggest that the trends may be general for oxides in fluorite structure.
- Both E_m^{Th} and E_m^O decrease with increasing temperature, potentially due to weakening atomic bonding. While E_d^O increases with increasing temperature because of thermally activated correlated recombination, E_d^{Th} decreases with increasing temperature due to the mild influence of correlated recombination.
- Regarding orientation dependence, E_d^{Th} and E_m^{Th} both follow the cubic symmetry. Additionally, for both E_d^O and E_m^O , a hidden asymmetry between [111] and $\bar{[111]}$ directions on the orientation map must be considered to fully describe the orientation dependence. The variation of E_d^O upon varying orientation, 26.4 eV to 246.9 eV, is much larger than that for E_d^{Th} , 30.42 eV to 120.36 eV.
- Further, it is found that the Coulomb interaction can reduce the migration barriers for charged point defects in FPs with short separation distances, thereby facilitating correlated recombination.

CRediT authorship contribution statement

Lin-Chieh Yu: Writing – review & editing, Writing – original draft, Visualization, Methodology, Investigation, Formal analysis, Data curation. **Shuxiang Zhou:** Writing – review & editing, Methodology. **Miaomiao Jin:** Writing – review & editing, Methodology. **Marat Khafizov:** Writing – review & editing, Supervision, Project administration, Methodology, Funding acquisition. **David Hurley:** Writing – review & editing, Supervision, Project administration, Funding acquisition. **Yongfeng Zhang:** Writing – review & editing, Writing – original draft, Supervision, Methodology, Investigation, Funding acquisition, Formal analysis, Conceptualization.

Declaration of competing interest

The authors declare that they have no known competing financial interests or personal relationships that could have appeared to influence the work reported in this paper.

Acknowledgment

This work was supported by the Center for Thermal Energy Transport under Irradiation (TETI), an Energy Frontier Research Center funded by the US Department of Energy, Office of Science, Office of Basic Energy Sciences. This research made use of the resources of the High Performance Computing Center at Idaho National Laboratory, which is supported by the Office of Nuclear Energy of the U.S. Department of Energy and the Nuclear Science User Facilities under Contract No. DE-AC07-05ID14517. Namely, all MD calculations were performed using the Sawtooth and Lemhi supercomputer at Idaho National Laboratory. The authors Yu and Zhang gratefully thank Professor William J. Weber for valuable discussions.

Appendix A. Supplementary data

Supplementary data to this article can be found online at <https://doi.org/10.1016/j.nme.2024.101774>.

Data availability

Data will be made available on request.

References

- [1] D.H. Hurley, et al., Thermal energy transport in oxide nuclear fuel, *Chem. Rev.* 122 (2022) 3711–3762.
- [2] W.E. Lee, M. Gilbert, S.T. Murphy, R.W. Grimes, Opportunities for advanced ceramics and composites in the nuclear sector, *J. Am. Ceram. Soc.* 96 (2013) 2005–2030.
- [3] *Thorium Fuel Cycle: Potential Benefits and Challenges*. (International Atomic Energy Agency, Vienna, 2005).
- [4] Boczar, P. G., Dyck, G. R., Chan, P. S. W. & Buss, D. B. *Recent Advances in Thorium Fuel Cycles for CANDU Reactors*. 104–120 <http://inis.iaea.org/search/search.aspx?orig.q=RN:33068572> (2002).
- [5] Baron, D. D. & Hallstadius, L. 2.19 - Fuel Performance of Light Water Reactors (Uranium Oxide and MOX). in *Comprehensive Nuclear Materials* (ed. Konings, R. J. M.) 481–514 (Elsevier, Oxford, 2012). doi:10.1016/B978-0-08-056033-5.00040-9.
- [6] Gomes, D. de S., de Stefani, G. L., Branco, F. & de Oliveira, V. ANALYSIS OF A PRESSURIZED POWER REACTOR USING THORIUM MIXED FUEL UNDER REGULAR OPERATION. (2019).
- [7] W.R. Deskins, et al., Thermal conductivity of ThO₂: Effect of point defect disorder, *J. Appl. Phys.* 129 (2021) 075102.
- [8] C.A. Dennett, et al., The influence of lattice defects, recombination, and clustering on thermal transport in single crystal thorium dioxide, *APL Mater.* 8 (2020) 111103.
- [9] Stoller, R. E. 1.11 - Primary Radiation Damage Formation. in *Comprehensive Nuclear Materials* (ed. Konings, R. J. M.) 293–332 (Elsevier, Oxford, 2012). doi:10.1016/B978-0-08-056033-5.00027-6.
- [10] K. Nordlund, et al., Primary radiation damage: a review of current understanding and models, *J. Nucl. Mater.* 512 (2018) 450–479.
- [11] G.H. Kinchin, R.S. Pease, The displacement of atoms in solids by radiation, *Rep. Prog. Phys.* 18 (1955) 1.

- [12] M.J. Norgett, M.T. Robinson, I.M. Torrens, A proposed method of calculating displacement dose rates, *Nucl. Eng. Des.* 33 (1975) 50–54.
- [13] J.F. Ziegler, M.D. Ziegler, J.P. Biersack, SRIM – The stopping and range of ions in matter (2010), *Nuclear Instruments and Methods in Phys. Res. Section B: Beam Interactions with Materials and Atoms* 268 (2010) 1818–1823.
- [14] P. Vajda, Anisotropy of electron radiation damage in metal crystals, *Rev. Mod. Phys.* 49 (1977) 481–521.
- [15] S.J. Zinkle, C. Kinoshita, Defect production in ceramics, *J. Nucl. Mater.* 251 (1997) 200–217.
- [16] M. Jiang, et al., An AIMD+U simulation of low-energy displacement events in UO₂, *J. Nucl. Mater.* 540 (2020) 152379.
- [17] H.Y. Xiao, Y. Zhang, W.J. Weber, Ab initio molecular dynamics simulations of low-energy recoil events in ThO₂, CeO₂, and ZrO₂, *Phys. Rev. B* 86 (2012) 054109.
- [18] R. Devanathan, T. Diaz de la Rubia, W.J. Weber, Displacement threshold energies in β -SiC, *J. Nucl. Mater.* 253 (1998) 47–52.
- [19] M. Robinson, N.A. Marks, G.R. Lumpkin, Sensitivity of the threshold displacement energy to temperature and time, *Phys. Rev. B* 86 (2012) 134105.
- [20] M. Robinson, N.A. Marks, K.R. Whittle, G.R. Lumpkin, Systematic calculation of threshold displacement energies: case study in rutile, *Phys. Rev. B* 85 (2012) 104105.
- [21] B. Dacus, B. Beeler, D. Schwen, Calculation of threshold displacement energies in UO₂, *J. Nucl. Mater.* 520 (2019) 152–164.
- [22] M. Bany Salman, M. Park, M.J. Banisalman, Atomistic study for the tantalum and tantalum-tungsten alloy threshold displacement energy under local strain, *Int. J. Mol. Sci.* 24 (2023) 3289.
- [23] N. Chen, D. Huang, E.R. Heller, D.A. Cardimona, F. Gao, Atomistic simulation of displacement damage and effective nonionizing energy loss in InAs, *Phys. Rev. Materials* 5 (2021) 033603.
- [24] J. Byggmästar, F. Granberg, K. Nordlund, Effects of the short-range repulsive potential on cascade damage in iron, *J. Nucl. Mater.* 508 (2018) 530–539.
- [25] K. Urban, N. Yoshida, The threshold energy for atom displacement in irradiated copper studied by high-voltage electron microscopy, *Philos. Mag. A* 44 (1981) 1193–1212.
- [26] M.J. Rahman, M.W.D. Cooper, B. Szpunar, J.A. Szpunar, Primary radiation damage on displacement cascades in UO₂, ThO₂ and (U_{0.5}Th_{0.5})O₂, *Comput. Mater. Sci.* 154 (2018) 508–516.
- [27] C. Meis, A. Chartier, Calculation of the threshold displacement energies in UO₂ using ionic potentials, *J. Nucl. Mater.* 341 (2005) 25–30.
- [28] L. Van Brutzel, J.-M. Delaye, D. Ghaleb, M. Rarivomanantsoa, Molecular dynamics studies of displacement cascades in the uranium dioxide matrix, *Phil. Mag.* 83 (2003) 4083–4101.
- [29] J. Soullard, A. Alamo, Study of deceleration of ions in a diatomic target. II. Calculation of the number of displaced atoms, *Radiat. Eff.* 38 (1978) 133–139.
- [30] J. Soullard, High voltage electron microscope observations of UO₂, *J. Nucl. Mater.* 135 (1985) 190–196.
- [31] S. Plimpton, Fast parallel algorithms for short-range molecular dynamics, *J. Comput. Phys.* 117 (1995) 1–19.
- [32] M.W.D. Cooper, M.J.D. Rushton, R.W. Grimes, A many-body potential approach to modelling the thermomechanical properties of actinide oxides, *J. Phys.: Condens. Matter* 26 (2014) 105401.
- [33] Zhou, S. et al. Improving empirical interatomic potentials for predicting thermophysical properties by using an irreducible derivatives approach: The case of thorium dioxide. Preprint at <http://arxiv.org/abs/2204.13685> (2022).
- [34] M.S. Daw, M.I. Baskes, Embedded-atom method: derivation and application to impurities, surfaces, and other defects in metals, *Phys. Rev. B* 29 (1984) 6443–6453.
- [35] P.M. Morse, Diatomic molecules according to the wave mechanics II. Vibrational levels, *Phys. Rev.* 34 (1929) 57–64.
- [36] R.A. Buckingham, J.E. Lennard-Jones, The classical equation of state of gaseous helium, neon and argon, *Proc. R. Soc. Lond. A* 168 (1937) 264–283.
- [37] M. Jin, et al., Assessment of empirical interatomic potential to predict thermal conductivity in ThO₂ and UO₂, *J. Phys.: Condens. Matter* 33 (2021) 275402.
- [38] Ziegler, J. F. Biersack, J. P. The Stopping and Range of Ions in Matter. in *Treatise on Heavy-Ion Science: Volume 6: Astrophysics, Chemistry, and Condensed Matter* (ed. Bromley, D. A.) 93–129 (Springer US, Boston, MA, 1985). doi: 10.1007/978-1-4615-8103-1_3.
- [39] V.V. Rondinella, T. Wiss, The high burn-up structure in nuclear fuel, *Mater. Today* 13 (2010) 24–32.
- [40] Y. Zhang, P.C. Millett, M.R. Tonks, X.-M. Bai, S.B. Biner, Preferential Cu precipitation at extended defects in bcc Fe: an atomistic study, *Comput. Mater. Sci.* 101 (2015) 181–188.
- [41] A. Stukowski, Visualization and analysis of atomistic simulation data with OVITO—the open visualization tool, *Modelling Simul. Mater. Sci. Eng.* 18 (2009) 015012.
- [42] K. Nordlund, M. Ghaly, R. Averback, Defect production in collision cascades in elemental semiconductors and fcc metals, *Physical Rev. B - Condensed Matter and Materials Phys.* 57 (1998) 7556–7570.
- [43] P.A. Burr, M.W.D. Cooper, Importance of elastic finite-size effects: neutral defects in ionic compounds, *Phys. Rev. B* 96 (2017) 094107.
- [44] C. Jiang, et al., Unraveling small-scale defects in irradiated ThO₂ using kinetic Monte Carlo simulations, *Scr. Mater.* 214 (2022) 114684.
- [45] G. Henkelman, H. Jónsson, Improved tangent estimate in the nudged elastic band method for finding minimum energy paths and saddle points, *J. Chem. Phys.* 113 (2000) 9978–9985.
- [46] G. Henkelman, B.P. Uberuaga, H. Jónsson, A climbing image nudged elastic band method for finding saddle points and minimum energy paths, *J. Chem. Phys.* 113 (2000) 9901–9904.
- [47] H.Y. Xiao, Y. Zhang, W.J. Weber, Stability and migration of charged oxygen interstitials in ThO₂ and CeO₂, *Acta Mater.* 61 (2013) 7639–7645.
- [48] L. Van Brutzel, A. Chartier, J.P. Crocombette, Basic mechanisms of Frenkel pair recombinations in UO₂ fluorite structure calculated by molecular dynamics simulations, *Phys. Rev. B* 78 (2008) 024111.
- [49] S. Moxon, et al., Structural dynamics of Schottky and Frenkel defects in ThO₂: a density-functional theory study, *J. Mater. Chem. A* 10 (2022) 1861–1875.
- [50] Y. Lu, Y. Yang, P. Zhang, Thermodynamic properties and structural stability of thorium dioxide, *J. Phys.: Condens. Matter* 24 (2012) 225801.
- [51] S.T. Murphy, M.W.D. Cooper, R.W. Grimes, Point defects and non-stoichiometry in thorium, *Solid State Ion.* 267 (2014) 80–87.
- [52] C.O.T. Galvin, M.W.D. Cooper, M.J.D. Rushton, R.W. Grimes, Thermophysical properties and oxygen transport in (Th_xPu_{1-x})O₂, *Sci Rep* 6 (2016) 36024.
- [53] B. Dorado, et al., First-principles calculations of uranium diffusion in uranium dioxide, *Phys. Rev. B* 86 (2012) 035110.
- [54] E. Vathonne, J. Wiktor, M. Freyss, G. Jomard, M. Bertolus, DFT + U investigation of charged point defects and clusters in UO₂, *J. Phys.: Condens. Matter* 26 (2014) 325501.
- [55] R. Perriot, et al., Atomistic modeling of out-of-pile xenon diffusion by vacancy clusters in UO₂, *J. Nucl. Mater.* 520 (2019) 96–109.
- [56] J.-P. Crocombette, Influence of charge states on energies of point defects and clusters in uranium dioxide, *Phys. Rev. B* 85 (2012) 144101.
- [57] L. Kittiratanawasin, R. Smith, B.P. Uberuaga, K. Sickafus, Displacement threshold and Frenkel pair formation energy in ionic systems, *Nucl. Instrum. Methods Phys. Res., Sect. B* 268 (2010) 2901–2906.
- [58] H.Y. Xiao, F. Gao, W.J. Weber, Threshold displacement energies and defect formation energies in Y₂Ti₂O₇, *J. Phys.: Condens. Matter* 22 (2010) 415801.
- [59] A. Annamareddy, J. Eapen, Fast anion defect recovery through superionic-type hopping displacements in UO₂ following radiation, *DDF* 375 (2017) 43–56.
- [60] H.Y. Xiao, Y. Zhang, W.J. Weber, Trapping and diffusion of fission products in ThO₂ and CeO₂, *J. Nucl. Mater.* 414 (2011) 464–470.
- [61] Y. Yun, P.M. Oppeneer, H. Kim, K. Park, Defect energetics and Xe diffusion in UO₂ and ThO₂, *Acta Mater.* 57 (2009) 1655–1659.
- [62] E.A. Colburn, W.C. Mackrodt, The calculated defect structure of thorium, *J. Nucl. Mater.* 118 (1983) 50–59.
- [63] P.S. Ghosh, A. Arya, N. Kuganathan, R.W. Grimes, Thermal and diffusional properties of (Th, Np)O₂ and (U, Np)O₂ mixed oxides, *J. Nucl. Mater.* 521 (2019) 89–98.
- [64] B. Liu, D.S. Aidhy, Y. Zhang, W.J. Weber, Theoretical investigation of thermodynamic stability and mobility of the oxygen vacancy in ThO₂–UO₂ solid solutions, *Phys. Chem. Chem. Phys.* 16 (2014) 25461–25467.
- [65] H.Y. Xiao, W.J. Weber, Oxygen vacancy formation and migration in Ce x Th 1-x O 2 solid solution, *J. Phys. Chem. B* 115 (2011) 6524–6533.
- [66] A.Y. Kuksin, D.E. Smirnova, Calculation of diffusion coefficients of defects and ions in UO₂, *Phys. Solid State* 56 (2014) 1214–1223.
- [67] M. Singh, T. Kumagai, A. El-Azab, A first-principles investigation of point defect structure and energetics in ThO₂, *J. Appl. Phys.* 132 (2022) 135111.
- [68] J.-P. Crocombette, D. Torumba, A. Chartier, Charge states of point defects in uranium oxide calculated with a local hybrid functional for correlated electrons, *Phys. Rev. B* 83 (2011) 184107.
- [69] K. Rickert, et al., Raman and photoluminescence evaluation of ion-induced damage uniformity in ThO₂, *Nucl. Instrum. Methods Phys. Res., Sect. B* 515 (2022) 69–79.
- [70] C.A. Dennett, et al., An integrated experimental and computational investigation of defect and microstructural effects on thermal transport in thorium dioxide, *Acta Mater.* 213 (2021) 116934.
- [71] V.I. Neeley, J.B. Gruber, W.J. Gray, F²⁺ centers in thorium oxide, *Phys. Rev.* 158 (1967) 809–813.
- [72] M. Sankowska, P. Bilski, B. Marczevska, Y. Zhydachevskyy, Influence of elevated temperature on color centers in LiF crystals and their photoluminescence, *Materials (Basel)* 16 (2023) 1489.
- [73] F. Karsai, et al., F²⁺ center in lithium fluoride revisited: comparison of solid-state physics and quantum-chemistry approaches, *Phys. Rev. B* 89 (2014) 125429.
- [74] T.R. Griffiths, J. Dixon, Electron irradiation of single crystal thorium dioxide and electron transfer reactions, *Inorg. Chim. Acta* 300–302 (2000) 305–313.
- [75] C.T. Walker, Thermal conductivity of some alkali halides containing F²⁺ centers, *Phys. Rev.* 132 (1963) 1963–1975.